A Developed and Characterized Orthotopic Rat Glioblastoma Multiforme Model

Sean Thomas

Thesis submitted to the faculty of the Virginia Polytechnic Institute and State University
in partial fulfillment of the requirements for the degree of

Master of Science
In
Biomedical Engineering

Scott. S. Verbridge
Rafael V. Davalos
John L. Robertson

24 September, 2020
Blacksburg, Virginia

Keywords: high-frequency irreversible electroporation, blood-brain barrier disruption, molecular targeted therapy, bioluminescent imaging, glioblastoma multiforme, tumor ablation, cancer therapy, electroporation, drug delivery, ablation, rat model

A Developed and Characterized Orthotopic Rat Glioblastoma Multiforme Model

Sean Thomas

ABSTRACT

This thesis project serves to fill experimental gaps needed to advance the goal of performing pre-clinical trials using an orthotopic rat glioblastoma model to evaluate the efficacy of high-frequency electroporation (H-FIRE) and QUAD-CTX tumor receptor-targeted cytotoxic conjugate therapies, individually and in combination, in selectively and thoroughly treating glioblastoma multiforme. In order to achieve this, an appropriate model must be developed and characterized. I have transduced F98 rat glioma cells to express red-shifted firefly luciferase, which will facilitate longitudinal tumor monitoring *in vivo* through bioluminescent imaging. I have characterized their response to H-FIRE relative to DI TNC1 rat astrocytes. I have demonstrated the presence of the molecular targets of QUAD in F98 cells. The *in vitro* characterization of this model has enabled preclinical studies of this promising glioblastoma therapy in an immunocompetent rat model, an important step before advancing ultimately to clinical human trials.

A Developed and Characterized Orthotopic Rat Glioblastoma Multiforme Model

Sean Thomas

GENERAL AUDIENCE ABSTRACT

Treating glioblastoma multiforme (GBM), a form of cancer found in the brain, has not been very successful; patients rarely live two years following diagnosis, and there have been no major breakthrough advances in treatment to improve this outlook for decades. We have been working on two treatments which we hope to combine. The first is high-frequency electroporation (H-FIRE), which uses electrical pulses to kill GBM cells while leaving healthy cells alive and blood vessels intact. The second is QUAD-CTX, which combines a toxin with two types of protein that attach to other proteins that are more common on the surface of GBM cells than healthy cells. We have shown these to be effective at disproportionately killing human GBM cells growing in a lab setting. Before H-FIRE and QUAD-CTX may be tested on humans, we need to show them to be effective in an animal model, specifically rats. I have chosen rat glioma cells that will behave similarly to human GBM and a rat species that will not have an immune response to them. I have made these cells bioluminescent so that we may monitor the tumors as they grow and respond to our treatments. I have also shown that QUAD-CTX kills these rat glioma cells, as does H-FIRE. Because of this work, we are ready to begin testing these two treatments in rats.

Acknowledgments

Thank you to my family, Kathy, Joram, Kelly, Pete, Peter John, Mary Sue, Deborah, Robert, Michael, Sue, and others, for forming me into a scholar.

Similarly, I must thank Dr. Melissa Moss, Dr. Yiying Wang, Dr. Nick Van der Munnik, Dr. Jeanne Stachowiak, Dr. Avinash Gadok, and Dr. Zachary Imam for forming me as a researcher before my time at Virginia Tech.

Thank you to the Laboratory for Integrative Tumor Ecology, Dr. Scott Verbridge, Dr. Megan Cox, Dr. Ishan Goswami, Dr. Jill Ivey, Dr. Anand Vadlamani, Barath Udayasuryan, Nastaran Alinezhadbalalami, Robert Bielitz, Savieay Esparza, Zerin Khan, Shuyu Zhang, Raffae Ahmad, and others.

I would also like to thank all of the BioElectroMechanical Systems Laboratory, Dr. Rafael Davalos, Dr. Yajun Zhao, Dr. Dan Sweeney, Dr. Elisa Wasson, Dr. Alex Hyler, Melvin Lorenzo, Kenneth Aycock, Philip Graybill, Natalie Beitel-White, Hongmei Liu, Josie Duncan and others.

Additional thanks is owed to all of the Munson Laboratory for Oncoengineering, Dr. Jennifer Munson, Dr. Chase Cornelison, Dr. Monet Roberts, Dr. Krishnashis Chatterjee, Caleb Stine, Kinsley Tate, Naciye Atay, Cora Esparza and others.

Further thank goes out to the Veterinary Team, Dr. John Robertson, Dr. John Rossmeisl, Jonathan Hinckley, Yukitaka Kani, Joy Adler, and others.

Additional thanks is due to the Traumatic Nerve Technologies Laboratory, Dr. Pamela VandeVord, Dr. Jess Boni, Fernanda Guilhaume-Correa, Michelle Dickerson, and others.

Thanks is due to many other individuals: Dr. Waldemar Debinski, Dr. Yong Woo Lee, Dr. Sheryl Coutermarsh-Ott, Dr. Anjaney Kothari, the David Brown Lab, Melissa Makris, Kandace Donaldson, Alyssa Huntington, and Rosalyn Hatlen to name a few.

Finally, I must thank those who funded this work, the National Institutes of Health (R01-CA213423 and P01-CA207206), the National Science Foundation (CBET-1652112), and the Virginia Tech-Wake Forest School of Biomedical Engineering and Sciences (Pratt Fellowship).

Table of Contents

Chapter 1: Introduction

Preamble

Cancer therapeutics has traditionally been a field of great research investment yielding marginal returns in patient outcomes. Perhaps this can be attributed to a tendency for tumor cells to infiltrate into healthy surrounding tissue and for their phenotype to evolve quickly and haphazardly. Perhaps this is why so few types of malignancies can reliably and universally be eliminated, particularly in the case of solid tumors. The easiest solution to the problem of tumor infiltration and heterogeneity is to destroy all nearby tissue indiscriminately. This is simply not an option for essential tissues and organs like the brain. To leave a potentially metastatic tumor intact is equally unacceptable. Given the phenotypic diversity of the typical malignancy that survives standard-of-care treatment, any one therapy will inevitably fail to eliminate every neoplastic cell, likely leading to recurrence. One strategy for success would be to leverage a fundamental difference between healthy tissue and all possible phenotypic profiles of a cancer cell; barring this, the greatest promise lies in the employment of multiple strategies, strategies that complement each other, in terms both of compatibility and of broad coverage of tumor phenotypic diversity, so that all that remains after treatment is healthy patient tissue.

The heterogenous nature of the tumor aside, a multi-pronged strategy has great merit. Civil and nuclear engineering abound with engineering redundancies in the name of promoting human safety. This tactic may be employed when treating solid tumors in cases in which it is appropriate. That appropriateness, is, however, limited, when off-target damage to healthy cells is inherent to the component treatments. Compounding effects of damage to healthy cells may overwhelm a patient just as cachexia and other cancer-mediated morbidities do. The key, then, is

to combine treatments that are selective and effective, so as to achieve the goal of total elimination of malignant cells with minimal damage to the natural structure and function of the surrounding tissue. All of these considerations are present and prominent in the treatment of glioblastoma multiforme.

Glioblastoma Multiforme

Glioblastoma multiforme (GBM) is the most common malignancy of the central nervous system, with over 12,500 patients diagnosed in 2019[1]. It is characterized by a highly variable phenotype[2] and a tendency towards invasion into adjacent tissue[3]. Treatments are severely limited in scope by the high medical and quality-of-life value of the surrounding brain parenchyma and in practicality by the blood-brain barrier (BBB), which has evolved to maintain brain homeostasis by limiting inward transport of bloodborne agents, generally to small, lipophilic molecules, at the cost of feasible administration of most drugs. This constitutes a challenge to treating GBM with chemotherapy. Nevertheless, chemotherapy, with radiotherapy, underlies the current standard of care, supplementing surgical resection[4]. The current standard of patient care is to resect the bulk tumor along with a reasonable margin of adjacent apparently healthy parenchyma, then apply temozolomide and concurrent radiotherapy in an attempt to neutralize infiltrative GBM cells[4,5]. Even with the current standard of care, patient life expectancy is no more than 18 months[6]. Only one out of fifteen patients survives five years past their diagnosis[1].

Clearly, there is much room for improvement in patient outcomes. Life expectancy has increased only about a month for every decade of glioblastoma research[7]. It can be induced from the results of previous attempts that modifications to the current standard of care will result in only marginal improvements in life expectancy. This supports the case for novel cancer therapies.

Irreversible Electroporation

One such therapy is irreversible electroporation (IRE). IRE is a therapy that uses the transient application of electric fields to ablate tumors. The ablation induced by IRE is dependent on electrical energy, rather than thermal energy[8], which spares protein-rich anatomical structures such as vasculature and connective tissue[9]. Tissue that is irreversibly electroporated is separated from surviving tissue that is only reversibly electroporated, by a minimal spatial transition zone[9]. This allows for precision in designing treatment plans to spare or kill cells, given the appropriate electrode configuration and treatment parameters, as well as knowledge of the electrical properties of the tissue. It has been used to treat prostate, pancreatic, and liver cancers[10,11,12]. Typically, IRE, as seen in these therapeutic contexts, consists of 50-100 μs high-voltage pulses delivered at 1 Hz over the course of one to a few minutes[13]. These pulses disrupt the equilibrium membrane voltage and cause intracellular ion polarization, such that the lowest energy state is realized by the disruption of phospholipid interactions to form intermittent gaps in the cell membrane, known as pores[13]. These pores allow for transmembrane passage of unconventional species, disrupting homeostasis. The duration and size of the membrane interruptions determine the distinction between reversible electroporation, which has been used to introduce therapeutic agents into the cell[15,16,17,18,19], and irreversible electroporation, wherein the transmembrane exchange represents too great a deviation from homeostatic equilibrium for the cell to sustain itself. As one might expect given the inherent pore induction, IRE has been shown to disrupt the BBB, which is formed by a layer of cells linked at the edges by a network of proteins that limits permeability. The permeation of the inner and outer phospholipid membranes of the cells causes the barrier to be disrupted; so too when its constituent cells shrink or die, or its constituent proteins detach or deform[20,21,22]. IRE affects the nervous system in another important way: in

certain cases, phasic overlap of IRE electric pulses can stimulate neurons and cardiac muscle cells to fire, an unintended effect that can result in physical dislodging of the delivery electrode(s) from the position ordained by treatment planning, as well as harm to the patient, which, in severe cases may include cardiac infarction[23]. Muscle relaxants can minimize these spasms in most cases[23].

An alternative approach to reducing neuromuscular excitation is high-frequency irreversible electroporation (H-FIRE). H-FIRE reduces the risk of nervous stimulation[24] by increasing the frequency of the pulses from 1 Hz to the order of 100 kHz. Stated more plainly, to translate an IRE treatment scheme to an H-FIRE treatment scheme, every 1 Hz 100 μs pulse is broken up into a burst of tens of shorter pulses, each on the order of 1 μs, with each pulse within a burst separated by a delay where no voltage is applied, also typically on the order of 1 μs. The other innovation to the pulse scheme that defines H-FIRE is the reversal of polarity with each alternating pulse. The negative polarity pulses are typically equal in duration to the positive polarity pulses. The nomenclature for the pulse scheme used in H-FIRE treatments consecutively lists the duration of the positive pulse, the duration of the inter-pulse delay, and the duration of the negative polarity pulse. For example, when H-FIRE begins with a 1 μs positive polarity pulse, a 5 μs delay, then a 1 μs negative polarity pulse, the pulse scheme is referred to as 1-5-1. Hence, when an IRE regimen with a consistent 1 Hz frequency is transformed into an H-FIRE regimen with a 1-5-1 pulse scheme, for that part of the second when energy is being applied, pulses are being delivered with a much higher frequency of 83,333 Hz.

There are many advantages associated with H-FIRE as a tumor treatment. For example, when treating 4T1 breast cancer models, H-FIRE mediated damage-associated molecular pattern (DAMP) signaling, creating 4T1 antigens, which induced a systemic immune response in a

mouse model that limited metastases[25]. In a pre-clinical study of spontaneous canine GBM, H-FIRE was shown to be effective at ablating clinically relevant tumor volumes, and patient outcomes were positive[26]. Additionally, H-FIRE has been shown in hydrogel tissue models to selectively target human GBM cells[27,28]. In other words, the lethal electric field threshold (EFT) magnitude was greater for normal human astrocytes (NHAs) than for U251 human GBM cells[27]. When NHAs and human GBM-like cells were co-cultured in collagen hydrogels, and H-FIRE was applied focally to the center of the hydrogels, there was a clear delineation of three zones along electric field contours: an outer zone in which all cells survived, an inner zone in which no cells survived, and an intermediate zone where only NHAs survived[28]. These results invite the further exploration of H-FIRE as a GBM therapy, predicated on the utility of its selectivity. H-FIRE was even more selective in the presence of ephrin A1. Pre-treatment with ephrin A1 increased the size of H-FIRE lesions and lowered the lethal EFT for human GBM U251 cells but not for healthy cells[29].

Molecular Targeted Therapy

Molecular targeted therapies are another strategy to selectively target GBM. Several genetic changes are required for somatic cells to transition from healthy to neoplastic. The finite pathways a cell may take to ultimate tumor formation dictate a tendency for a few specific genes to be overexpressed in a given type of cancer. When these overexpressed genes code for cell surface proteins, this overexpression may be taken advantage of in the creation of a therapy that targets those proteins. The lab of our collaborator, Dr. Waldemar Debinski at Wake Forest University, has determined that protein targets overexpressed in GBM include EPH A2, IL-13Rα2, and Fra-1; 95% of GBM tumors investigated overexpress at least two of these receptors[30].

EPH A2 is one of a class of receptors called EPHs that are bound by ephrins before downstream pathway activation. EPH-ephrin interactions are possible for many combinations, usually within the same subclass (ephrin class A with EPH class A and ephrin class B with EPH class B), and their effects vary widely according to multiple factors: the specific EPH molecule, the specific ephrin molecule, and even cell type[31]. Further complicating these interactions is the possibility for both forward signaling, wherein an ephrin binds an EPH on the cell surface and activates a pathway within that cell, and reverse signaling wherein an EPH on that same cell binds an ephrin on the surface of another cell and effects a signal induction on the second cell[31]. EPH-ephrin signaling is involved in many processes, including stem cell regulation and development, cytoskeletal remodeling, and, notably, cancer[31]. Besides EPH A2, EPH A3 and EPH B2 are also over-expressed in many glioblastoma tumors, and all three may be targeted with a common ligand, ephrin A5[32]. In cancer, higher EPH A2 and EPH A3 levels are associated with poorer patient prognoses[31], although the implication of high EPH B2 expressions is more nuanced. In glioma, EPH B2 activation is associated with migration, growth, and invasion[33]. Both ephrin A5 and ephrin A1 have been bound to cytotoxins and used to kill GBM cells[32,34].

Ephrins are not alone as useful ligands for targeting GBM. IL-13 is involved in extracellular matrix- and immune response-related processes, but of primary concern here is its role in cancer[35]. IL-13 cell-surface binding follows three archetypes[36,37]. In the first, IL-13 binds to IL-13Rα1, which forms a heterodimeric complex with IL-4Rα, leading to the downstream proliferative STAT6 pathway associated with apoptotic resistance. In the second, IL-13 binds to a lone transmembrane IL-13Rα2, leading to pro-metastatic pathways. Indeed, in many cancers, IL-13Rα2 expression is correlated with metastatic activity in tumors[37]. In the third, IL-13 binds to a cleaved variant of IL-13Rα2 that activates nothing, as it is a decoy receptor; this decoy effect

is aided by IL-13Rα2's higher affinity for IL-13 relative to IL-13Rα1[36,37]. The Debinski group has discovered a modification to IL-13 that creates an increased disparity between these relative affinities; this modified form is called IL-13.E13K[38,39].

To simultaneously target EPH A2, EPH A3, EPH B2, and IL-13Rα2, the Debinski lab has created a construct consisting of two of these IL-13.E13K molecules connected via methyl groups to two ephrin A5 molecules, dubbed "QUAD", which will target the four receptors of IL-13 and ephrin A5 ligands widely overexpressed in GBM. The QUAD construct can be conjugated to bacterial toxins, such as Pe38QQR, modified *Pseudomonas* exotoxin, or chemotherapeutic agents, such as WP396, modified doxorubicin, so that the cells that its ligands target may then be killed[7]. In *in vitro* experiments and in spontaneous GBM canine patients using convection-enhanced delivery, QUAD-Pe38QQR has been shown to potently kill GBM[40]. Thus, the remaining obstacle to QUAD-CTX-driven GBM treatment is its delivery across the BBB.

Combinatorial Therapy

There are several strategies that have shown success in bypassing or disrupting the BBB, but of particular note for the purposes of this project is IRE. As previously noted, IRE has been shown in multiple studies to disrupt the BBB[20,41,42]. H-FIRE, a subset of IRE, targets GBM cells more selectively in the presence of ephrin A1[29], presumably through interaction with its primary receptor, EPH A2[43]. Ephrin A5, the secondary ligand for EPH A2[43], retains its binding affinities and functionality when incorporated into QUAD[40]. All these considerations taken together suggest that H-FIRE and QUAD-CTX may not only perform effectively individually as GBM treatments but may also increase each other's effectiveness as a GBM therapy.

We propose to develop a therapy combining these two treatments that uses high-frequency pulsed electric fields to ablate the central tumor mass and disrupt the BBB at and radially farther than the tumor margins, allowing QUAD-CTX to enter the brain parenchyma, where it will deliver its payload overwhelmingly to tumor cells at the margins of irreversible electroporation and beyond, to malignant cells that have infiltrated more deeply into the surrounding parenchyma. In the longer term, H-FIRE-mediated DAMP signaling might act as a third targeted attack against any potential remnants of the tumor, and delayed doses of QUAD-CTX may be delivered intravenously, creating a gradient such that areas closer to the former tumor centroid will have had greater exposure to QUAD-CTX due to longer-lasting local blood-brain barrier disruption (BBBD).

Prior to use in humans, this strategy must be tested in animal models. Prior to that, this model will need to be developed, and multiple questions must be answered. While there have been some studies wherein IRE is used to disrupt the BBB, a better understanding of the effectiveness and duration of BBBD by high-frequency pulsed electric fields is crucial for planning treatments that use high-frequency pulses for therapeutic BBBD. While ephrin A1 has decreased the lethal H-FIRE EFT in U251 cells but not normal human astrocytes, cells derived from human sources, QUAD uses ephrin A5 bound to a larger construct, so it would be a non-trivial assumption that QUAD would have the same effect on lethal EFTs, particularly in rat cells. As a rat model will be used to test these therapies, it must also be determined whether the effectiveness of H-FIRE and QUAD-CTX seen in human cells is mirrored in the rodent model, and to what extent. In this thesis, I create such a model and describe the effectiveness of QUAD-CTX and H-FIRE in the context of this model, both individually and in combination.

Chapter 2: Model Development

Introduction

When choosing a cell line for the tumor component of the model, C6, F98, 9L, and RG-2 cell lines were all considered, but ultimately, F98 cells were selected, as they provided the widest set of advantages for the purpose of our study. The low-to-non-immunogenic nature of their implantation in immunocompetent Fischer rats[44] leaves open the possibility for investigating DAMP signaling in response to potential H-FIRE-mediated immune activation. Fischer rats were therefore chosen as the host component of the model. Their highly infiltrative nature[45] should facilitate a radial survey of focal treatment efficacy, providing data useful for planning treatments with an outer zone of selectivity. Finally, their proven track record in bioluminescent imaging[46,47,48] (BLI) bodes well for our intention not merely to conduct an endpoint study of tumor growth and treatment response but also to monitor tumor dynamics longitudinally.

As for how the host and tumor elements will be combined, the pre-clinical model will use orthotopic tumor inoculation, since studying high-frequency pulsed electric fields and their potential BBB-disruptive effects is instrumental to the study. In accord with a well-characterized F98-Fischer rat orthotopic model[49], 10,000 F98 cells in 5 µl of phosphate buffered saline (PBS) will be injected into the brain 1 mm posterior to the bregma, 2.5 mm to the right of the midline at a depth of 3 mm at a rate of 1 µl/min. The needle will be held at the same position for 120 seconds following complete injection so that F98 cells are not introduced along the dorsal-ventral insertion axis.

With these considerations noted, I sought to create a bioluminescent strain of F98 cells, which will be used to characterize the effectiveness of QUAD-CTX and H-FIRE in the rodent model. In this chapter, I seek to maximize the bioluminescent signal intensity of the new F98 strain so that it is well-suited to *in vivo* bioluminescent imaging.

Methods

Cell Culture

F98 undifferentiated *rattus norveticus* glioma cells (ATCC) and DI TNC1 *rattus norveticus* phenotype 1 astrocytes (ATCC) were cultured in Dulbecco's Modified Eagle's Medium (ATCC) with 100 units/ml penicillin, 100 μg/ml streptomycin (Gibco), and 10% added fetal bovine serum (Tissue Cultures Biological 101). Cells were passaged when observed to be at 70% or higher confluency, or roughly every 60 hours. F98 cells were passaged by removing the media, washing with 0.05% Trypsin-EDTA (Gibco), then incubating in 2 ml 0.05% Trypsin-EDTA for five minutes before neutralization with 6 ml media and seeding at a 1:10 dilution.

Lentiviral Plasmid Transduction

F98 cells were seeded at various densities (5,000 – 50,000 cells/well) into 24-well plates and monitored in stages to determine optimum seeding density and other conditions for transduction with a lentiviral vector to express a plasmid coding for red-shifted firefly luciferase, enabling bioluminescence in the presence of luciferin, as well as green fluorescent protein (GFP) as a non-luminescent reporter and a puromycin resistance factor to facilitate selection for plasmid expression (pLL-EF1a-Luciferase-T2A-Puro Lenti-Labeler Lentivector Virus, Systems Biosciences Incorporated). This was to seek a balance between the prescribed viral incubation times, the prescribed cell seeding density, the rapid proliferation of the F98 cells, and the threat

of exhaustion of resources within the well over the prescribed exposure time of the lentivirus. The transduction procedure ultimately implemented for one strain ($F98_{Luc,MOI=20}$) was as follows: 50,000 cells were seeded into a well of a 24-well plate and incubated for 18-24 hours before adding approximately $2 * 10^6$ IFUs of lentivirus for an estimated multiplicity of infection (MOI) of 20, based off of the previously observed population doubling time for our strain of F98 cells. As cells tended to cluster in the center, with this effect increasing over the course of their incubation, the following seeding technique was used to minimize this: 500 µl of cells were ejected while moving the tip laterally above the surface of the well; if the surface was fully sampled during the course of pipetting, ejection was repeated at the edges of the well. After each well was filled, the plate would be moved towards and away from the edge of the hood five times then towards the right and towards the left of the hood five times, ensuring that the media settled to the point of lacking visible movement of media before proceeding to the next agitation. After all wells were filled, the plate would be agitated forward-and-back 5 times, right-and-left 5 times; then 5 repeats of a sequence consisting of 1x forward-back agitation followed by 1x right-left agitation would be applied, again with media settling fully between agitations. The plate was then allowed to sit in the hood for 15 minutes before careful cart-mediated transfer to the incubator (310 K, 5% CO_2, as in every other subsequent instance), at which point the agitation procedure previously employed following complete seeding of the plate would be repeated. 48 hours after exposure to virus, the media was removed and replaced with 2.5 µg/ml puromycin (Millipore Sigma) in media, in which cells were incubated for 24 hours before they were transferred to T25 cell culture flasks in puromycin-free media. This strain, wherein the MOI was 20, denoted as $F98_{Luc,MOI=20}$, was one of 5 strains to be tested, along with two exposed to the same conditions, except with an MOI of 10 ($F98_{Luc,MOI=10}$) or 5 ($F98_{Luc,MOI=5}$). Two strains were

transduced earlier as part of the cell seeding and growth condition optimization trials: $F98_{Luc,C6}$ from 50,000 cells initially seeded, allowed to incubate for 24 hours before transduction at an MOI of 5, and incubated with virus for 72 hours before 24 hours of puromycin (2 μg/ml) selection and final harvesting; and $F98_{Luc,A6}$, which underwent the same conditions as $F98_{Luc,C6}$ except for starting from an initial 12,500 cells and receiving a supplement of 200 μl fresh media to the standard 500 μl well coverage volume 24 hours into the viral incubation stage. The various strains were cultured until robust proliferation was observed, then frozen for future use.

Strain Selection

On the basis of preliminary transduction efficiency assays, including luminometric plate reading and flow cytometry, in which $F98_{Luc,MOI=20}$, $F98_{Luc,MOI=10}$, and $F98_{Luc,C6}$ consistently showed marginally to somewhat higher expression than $F98_{Luc,MOI=5}$ and $F98_{Luc,A6}$, the evaluation process was narrowed down to the former three strains. The bioluminescence of these strains was measured by plating in a 24-well opaque-sided glass-bottom plate (Perkin-Elmer) varying numbers of cells on a logarithmic scale in quadruplicate, incubating them overnight, replacing their media with 150 μg/ml D-luciferin (Gold Biotechnology) in growth medium, measuring luminescence using the In Vivo Imaging System (IVIS) (Perkin Elmer), designating each well as a region of interest, plotting luminescent signal against cell number, and applying to the data a linear fit, the slope of which describes the luminescence of the strain in units of photons/s/cell. On the basis of these additional preliminary probes, the $F98_{Luc,MOI=20}$ strain was selected to undergo further modification.

Luminescent Signal Optimization: Puromycin Selection

The luminescent signal observed through IVIS from the $F98_{Luc,MOI=20}$ strain immediately after transduction was insufficient for signal to be detected with adequately low exposure time and adequately high resolution when attenuated by the skull and soft tissue dorsal to the brain of a Fischer rat, the threshold for which is 1,000 photons/s/cell. To address this, 10 μg/ml puromycin was added to the growth medium of the $F98_{Luc,MOI=20}$ strain following one passage post-thaw before plating for luminescent signal evaluation in the IVIS. This proved insufficient, so cells were seeded into a glass-bottom plate, allowed to adhere in an incubator overnight before their growth medium was exchanged for growth medium containing varying puromycin concentrations: 0, 0.2 μg/ml, 0.8 μg/ml, 2 μg/ml, 3 μg/ml, 4 μg/ml, 6 μg/ml, 8 μg/ml, 10 μg/ml, 13 μg/ml, 17 μg/ml, and 20 μg/ml. Cells were monitored daily using an EVOS FL Auto 2 microscope (Invitrogen), allowing for instantaneous comparison between brightfield phase contrast imaging, by which all cells were visible, and green fluorescent channel imaging of the same field, which displayed GFP-expressing cells. Cell growth and fluorescence was monitored over seven days, at which point endpoint evaluations were conducted: measurement of luminescent signal using the IVIS and quantification of the cells following trypsinization (250 μl of 0.05% Trypsin-EDTA), 3:1 dilution and trypsin neutralization with growth medium, removal from well, mixing, and cell density calculation from 10 μl of solution on a hemacytometer (Hausser Scientific). Various puromycin concentration treatments were evaluated on three criteria: the ubiquity of GFP expression among cells observed in phase contrast, the growth inhibition in response to the puromycin dose, and the intensity of the luminescent signal.

As 20 μg/ml puromycin was deemed to be the most effective dose, $F98_{Luc,MOI=20}$ cells were therefore further passaged and grown in medium containing 20 μg/ml Puromycin, before being

seeded in glass-bottom 24-well plates and imaged in the IVIS, yielding a value for luminescence per cell. The measured value was still lower than the target luminescent signal for *in vivo* bioluminescent imaging, by a factor of 4.4.

Luminescent Signal Optimization: Fluorescence-Activated Cell Sorting

$F98_{Luc,MOI=20}$ cells were passed through a flow cytometer (Guava 12HT, Millipore Sigma), where GFP expression was given by event count. The average green fluorescent signal intensity of the GFP+ cells was determined and multiplied by 4.4. The presence of cells above this GFP expression benchmark was observed, which supported the possibility of a subpopulation of $F98_{Luc,MOI=20}$ cells with 4.4 times higher than average luciferase expression. The underlying assumption is that a 4.4-fold increase in green fluorescent signal intensity corresponds to a 4.4-fold increase in luminescent signal intensity.

Therefore, fluorescence-activated cell sorting (FACS) (FACSAria I, BD Biosciences) was used to select the population for which the lower bound of green fluorescent signal intensity was 4.4x the average signal for GFP+ living cells. Cells recovered through this method were cultured, expanded, and frozen. Subsequent IVIS luminescence readings showed cellular luminescence to be greater than the target for luminescent signal. Henceforth, this subpopulation was denoted as $F98_{BL}$.

Pathogen Testing

Rodent pathogen testing of the $F98_{BL}$ cells was outsourced to Charles River Research Animal Diagnostic Services. Polymerase chain reaction (PCR) tests were conducted for HANT (Hantavirus Hantaan), IDIR, K Virus, LCMV, LDV, MAV 1 & 2, MCMV, MHV, Mouse Parvovirus (MPV/MVM), Mousepox (Ectromelia), MNV, MRV (EDIM), MTLV, POLY, PVM,

RCMV, RCV/SDAV, REO, Rat Parvovirus (RPV), RTV, SEND, SEO (Hantavirus), TMEV/GDVII, Vesivirus, *Mycoplasma* Genus, and *M. pulmonis*.

Results

Lentiviral Plasmid Transduction

Following transduction and initial puromycin selection (2.5 μg/ml puromycin for 24 hours within the well in which they were transduced), $F98_{Luc,MOI=20}$ cells were plated, incubated overnight, exposed to 150 μg/ml D-luciferin in growth medium, and imaged using the IVIS. They emitted a bioluminescent signal of a 62.71 ± 2.02 photon/s/cell (Figure 2.1).

Luminescent Signal Optimization: Puromycin Selection

As this was insufficient, they were exposed to 10 μg/ml puromycin over the course of one passage. The resultant measured signal had increased to 111.76 ± 3.19 photons/s/cell (Figure 2.1). This too fell short of the target luminescence of 1,000 photons/s/cell, so the effects of various puromycin doses (0, 0.2, 0.8, 2, 3, 4, 6, 8, 10, 13, 17, and 20 μg/ml) were evaluated in an effort to determine a dose which would maximize cellular luciferase expression while allowing the cells to maintain sufficient long-term viability.

The puromycin-free medium yielded somewhat scattered GFP expression among cells (Figure 2.2A). Exposure to 0.2, 0.8, and 2 μg/ml puromycin led some cells to express GFP. For doses between 3 and 10 μg/ml, most cells expressed GFP. 13 and 17 μg/ml puromycin induced nearly all cells visible with contrast microscopy to express GFP, though some exceptions could be found. $F98_{Luc,MOI=20}$ cells exposed to 20 μg/ml puromycin, however, universally expressed GFP, at least as observed in cells that appeared viable (Figure 2.2A). Cell count was also evaluated for

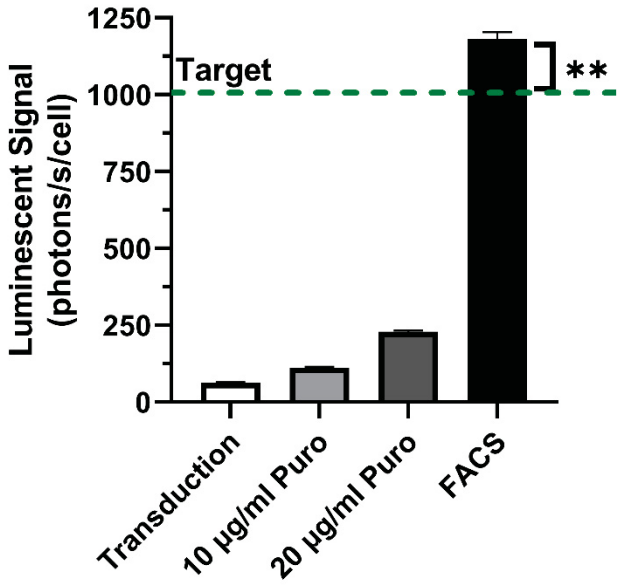

Figure 2.1. $F98_{Luc,MOI=20}$ cells after successive stages of selection. $F98_{Luc,MOI=20}$ cells were treated with 10 µg/ml puromycin before being treated with 20 µg/ml puromycin; finally fluorescence activated cell sorting selected for the $F98_{Luc,MOI=20}$ cells with the highest GFP signal. After every stage of selection, luminescent signal increased, until finally it was higher than the target ($p < 0.01$).

the various doses, with a plateau around 1,300,000 cells/well observed for all doses up to 2 µg/ml and seen as high as 8 µg/ml, before decreasing until another plateau observed at ~750,000 cells/well for 17 and 20 µg/ml (Figure 2.2B). As for cellular luminescence observations, there was generally observed a steady increase from ~45 photons/s/cell for the no puromycin and 0.2 µg/ml puromycin conditions up to ~225 photons/s/cell for the 20 µg/ml condition (Figure 2.2C). The main line of $F98_{Luc,MOI=20}$ cells was therefore passaged and had its growth medium replaced with 20 µg/ml puromycin for two consecutive passages, totaling 7 days, before plating and additional luminescence tests demonstrated an increased cellular luminescence: 228.27 ± 4.50 photon/s/cell (Figure 2.1).

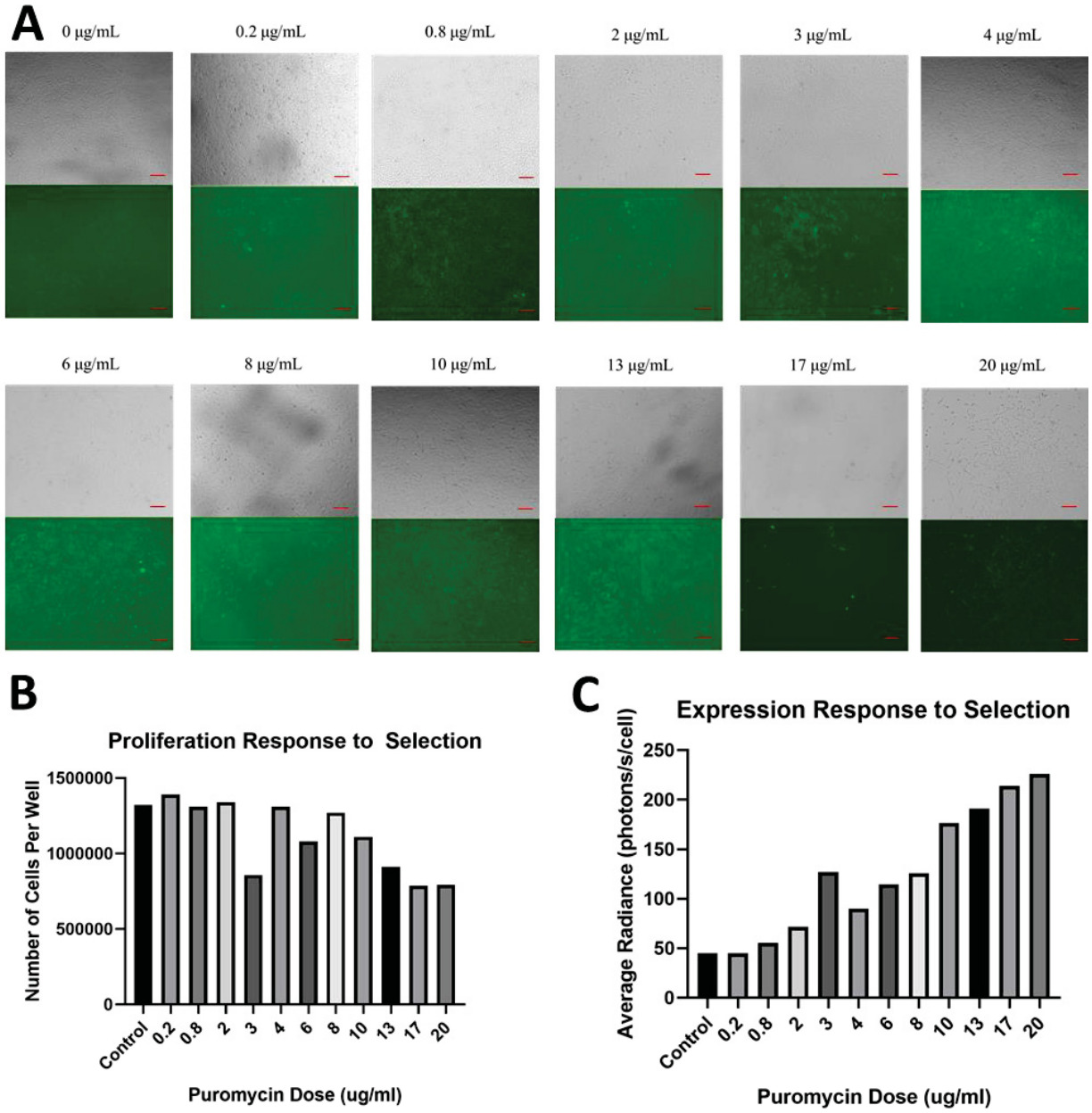

Figure 2.2. $F98_{Luc,MOI=20}$ response to varying doses of puromycin. By day 7, most cells treated with puromycin expressed GFP, but only those treated with 20 µg/ml puromycin universally expressed GFP; scale bar denotes 100 µm (A). With increasing puromycin dose, $F98_{Luc,MOI=20}$ generally decreased in cell number (B), but increased in luminescent signal (C).

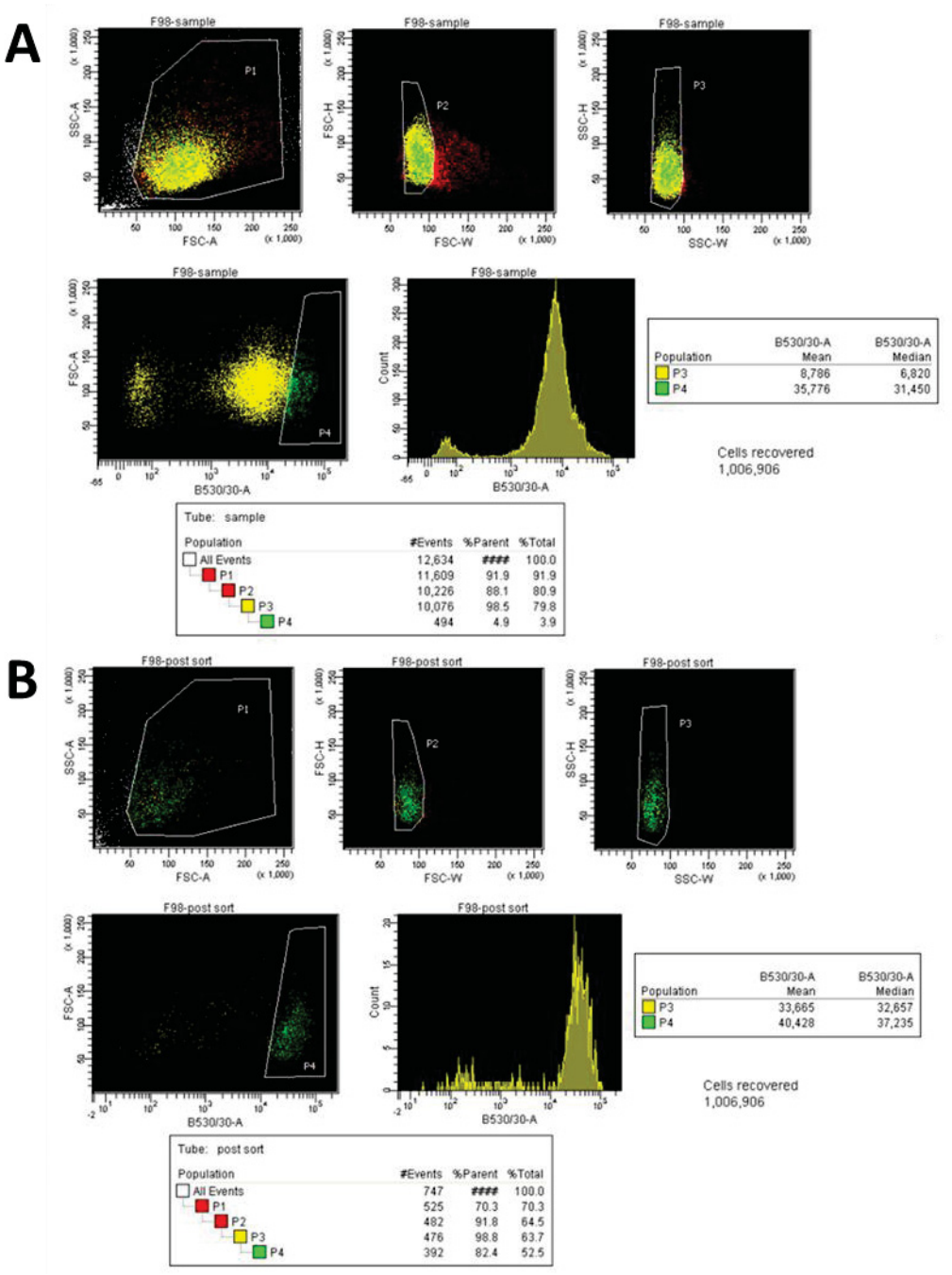

Figure 2.3. Fluorescence-activated cell sorting to select for high GFP expression. $F98_{Luc,MOI=20}$ cells were sorted to include all live cells, then to include the cells with GFP signal 4.4 times higher than the modal GFP+ cell (A). Resampling the final selection of cells showed that 82.4% of live $F98_{Luc,MOI=20}$ cells exceeded the GFP expression threshold once again (B).

Luminescent Signal Optimization: Fluorescence-Activated Cell Sorting

Finally, FACS was employed, yielding the top 4.9% of viable F98 cells by green fluorescent signal, constituting a population with 4.4 times the green fluorescent signal intensity of the average GFP-expressing cell (Figure 2.3A). A subsample of this population was tested to see whether these cells would fall into the same sorting parameters when passed through a second time, and 82.4% of viable F98 cells were found to fit into the same green fluorescent parameter constraints (Figure 2.3B). The luminescent signal measurement protocol was repeated for this subpopulation of $F98_{Luc,MOI=20}$, yielding a luminescent signal of 1,180.69 ± 23.28 photons/s/cell (Figure 2.1). This was significantly higher than the target value of 1,000 photons/s/cell ($p < 0.01$, one-sample one-tailed t test). Henceforth, this subpopulation was referred to as $F98_{BL}$.

Pathogen Testing

Cell pathogen testing, outsourced to Charles River Research Animal Diagnostic Services, showed the $F98_{BL}$ cells to be free from all pathogens for which PCR testing was conducted.

Discussion

Pathogen testing was conducted on the $F98_{BL}$ cells that will be used to inoculate the Fischer rat subjects. All viruses tested for were found not to be present in the $F98_{BL}$ cells frozen in reserve for tumor inoculation. The absence of rat pathogens is key, both to avoid confounding variables in *in vivo* studies and to avoid causing undue harm to the subjects.

The process of refining the $F98_{Luc,MOI=20}$ population into the $F98_{BL}$ subpopulation involved incubation with 10 μg/ml puromycin, followed by incubation with 20 μg/ml puromycin, and finally selection of the brightest plasmid-expressing cells using FACS.

Three factors were present in the decision to set the second puromycin dose to 20 μg/ml: the luminescent signal, the stress imposed on the cells by the puromycin, and the proportion of cells that were observed to express the plasmid. Obviously, maximizing the luminescent signal was the primary objective, but the other measures cannot be ignored. If a high puromycin dose stressed the $F98_{Luc,MOI=20}$ cells to the point where their growth was stunted and they were no longer viable in cell culture and could not be expanded, then tumor inoculation could never be realized and that puromycin dose would be of no use in developing the rodent-tumor model. Incidentally, this was also the rationale for monitoring and evaluating the growth and signal of the other transduced F98 populations besides $F98_{Luc,MOI=20}$: ensuring that the lentiviral load would not overwhelm the cells' short-term or long-term viability was essential for their ultimate use in the *in vivo* tumor model.

The proportion of cells seen to be expressing GFP was also deemed a critical consideration. Cells which did not possess or adequately express the plasmid would pose a threat to the long-term stability of any $F98_{BL}$ cell line, both in culture and, particularly, post-implantation, where there are fewer opportunities for phenotypic control and the effects of low or variable luminescent signal have a greater negative impact on the project. Given the degree to which phenotypic drift has been observed over even low single-digit passage divergence in standardized cell culture[50], it is by no means unimaginable that minute metabolic efficiency advantages by no-plasmid copy and low-plasmid copy cells over higher signal cells could propagate in *in vitro* culture and the tumor microenvironment alike, limiting tumor detectability and leading to inconsistent results. While the 13 μg/ml and 17 μg/ml puromycin treatments had only token non-GFP-positive cells, none were observed for the 20 μg/ml treatment. 100% selectivity for plasmid expression is a rare feat, and the entire surface of the well was not exhaustively sampled, so actual plasmid

expression may be lower. Indeed, flow cytometry and FACS showed a small population of non-GFP-expressing $F98_{Luc,MOI=20}$ cells. The long exposure to a higher-than-typically recommended dose of puromycin, however, increases the chances of successful selectivity. As a cell population with universal plasmid expression would vastly reduce the possibility of phenotypic drift, these observations supported the use of 20 μg/ml puromycin treatment.

This treatment also showed the highest luminescent signal per cell, impressive as it was even measured to be higher than the 17 μg/ml treatment, which had a nearly identical measured cell count.

Those cell counts were, however, the lowest of all doses administered, which raises the question of viability. The experiment was designed to monitor the cells over seven days, approximately the length of two puromycin-free passages in conventional F98 cell culture practice. While the higher puromycin dose wells did not reach full confluency, which from the plateau observed in Figure 2.2B, we can presume is ~1,300,000 cells, they did show sustained, observable, and sufficient growth, growth whose multiplication of cell density, when translated to a culture flask, would allow for comfortable passaging after a slightly longer time. The concerns regarding cell viability were more than offset by the extremely promising universally observed GFP expression and relatively high luminescent signal; accordingly, 20 μg/ml puromycin was selected as the appropriate dose with which to treat $F98_{Luc,MOI=20}$.

Still, the luminescent signal fell below the target of 1,000 photons/s/cell. The luminescent signal of the cells was 228.27 ± 4.50 photons/s/cell, below that target by a factor of approximately 4.4. It can reasonably be assumed that a 4.4-fold increase in green fluorescent signal would roughly correspond to a 4.4-fold increase in luminescent signal. After flow cytometry was used to observe the distribution of GFP signal intensity and it was confirmed that a non-trivial proportion

(~13%) of cells could be found at 4.4 or more times the average cell green fluorescence signal intensity of a population that excluded cells that did not express GFP, FACS was employed such that the lower boundary for the final sorting event was set to roughly 4.4x the modal GFP expression. Notably, this would mean that, in theory, the lower extreme of luminescent signal would sit at approximately 1,000 photons/s/cell, implying a mean luminescent signal higher than that. Resampling a small proportion of that 4.4-times-higher-than-average-bounded subpopulation showed that 82.4% of viable cells fell within the signal parameters after a second pass, with some cells falling in the non-GFP-expressing range. This low number was a matter of small concern, though it was mitigated by considerations that FACS does not offer a typical environment and that the cells had undergone multiple stressors leading up to the resampling.

Nevertheless, the 1,180.69 ± 23.28 photons/s/cell luminescent signal observed from these cells is a cause for confidence in $F98_{BL}$ as appropriate for a tumor model that makes use of BLI. This signal intensity is much higher than the one reported in Bryant *et al.*[46], in which the F98 BLI model was first implemented. While their *in vitro* luminescence data cannot be expressed with absolute certainty, as their luminescence data is reported in photons/s/cm^2 with no area explicitly mentioned, their highest cell count for which luminescence is measured *in vitro* is 100,000, which eliminates a 96-well plate. Therefore, the measurements were performed over an area between 1.1 cm^2 (48-well plate) and 9.6 cm^2 (6-well plate), though given that their data was performed in triplicate for 8 distinct cell counts, a 24-well plate seems most likely (1.9 cm^2). I performed a linear regression on their table-listed data, which yielded a trendline with a slope of 8.97 ± 0.32 photons/s/cm^2/cell, which means the likeliest luminescent signal intensity is 17.05 ± 0.61 photons/s/cell, though values between 9.87 ± 0.36 photons/s/cell (48-well plate) and 86.12 ± 3.10 photons/s/cell (6-well plate) are also possible. They compensate for their lower signal

intensity with a longer *in vivo* imaging exposure time, namely 15 minutes. The manufacturer recommendations for *in vivo* BLI are to limit exposure times to below 5 minutes to avoid capturing time-dependent physiological changes in the average. Similarly, Huang, when developing a bioluminescent F98 population for evaluating a radiotherapy with BLI, used exposure times of 10 minutes for inoculated tumors; notably, by my back-calculations from their graphically displayed *in vitro* luminescent signal data, their luminescent signal was in the single digits (the exact value I calculated was 5.3 photons/s/cell, though the logarithmic y scale could have introduced minor error into my approximations; those trying to replicate my post-analysis should keep in mind that mean photon count extends over a 60 second exposure time)[47]. This too is a lower luminescent signal intensity than seen in the $F98_{BL}$ cells I have developed for this project.

The $F98_{BL}$ line that I have developed presents the advantages that come with a higher signal: higher resolution, lower gain requirements, and shorter exposure times. The fruits of these advantages may include the ability to detect smaller volumes of tumor cells than may otherwise have been possible *in vivo*, lower rodent patient stress from reduced handling, and lower patient risk from decreased anesthesia exposure times. The importance of an adequate luminescent signal intensity cannot be understated.

Chapter 3: Effectiveness of QUAD-CTX Against $F98_{BL}$ Cells

Introduction

To determine the effectiveness of QUAD-CTX in our rodent model, we began by testing the gene expression of our tumor cell component, $F98_{BL}$ cells, to determine which targets of QUAD are present in $F98_{BL}$. If none were present, this would be cause for rethinking the tumor component of the model. This is unlikely given that QUAD targets four distinct receptors that are each commonly expressed in GBM, but it nevertheless must be tested. $F98_{BL}$ cells were studied alongside DI TNC1, an astrocytic rat cell line that represents the cells of the healthy bulk tissue that will be found in the host brain parenchyma. Beyond quantification of transcription, we were also interested in the presence of protein on the cell surface. We therefore used immunocytochemistry to visualize presence and localization of one of QUAD's targets, EPH A2. Finally, we measured $F98_{BL}$ and DI TNC1 viability in response to various doses of QUAD conjugated to WP396, a modified form of doxorubicin.

Methods

Cell Culture

$F98_{BL}$ cells (developed from F98 cells, ATCC) and DI TNC1 *rattus norveticus* phenotype 1 astrocytes (ATCC) were cultured in Dulbecco's Modified Eagle's Medium (ATCC) with 100 units/ml penicillin, 100 µg/ml streptomycin (Gibco), and 10% added fetal bovine serum (Tissue Cultures Biological 101). Cells were passaged when observed to be at 70% or higher confluency,

or roughly every 48 hours for DI TNC1 cells and every 60 hours for $F98_{BL}$ cells. DI TNC1 cells were passaged by removing the media, washing with 0.25% Trypsin-EDTA (Quality Biological), then incubating in 2 ml 0.25% Trypsin-EDTA for five minutes before neutralization with 6 ml media and seeding at a 1:6 dilution. $F98_{BL}$ cells were passaged by removing the media, washing with 0.05% Trypsin-EDTA (Gibco), then incubating in 2 ml 0.05% Trypsin-EDTA for five minutes before neutralization with 6 ml media and seeding at a 1:10 dilution.

Polymerase Chain Reaction

RNA was isolated from $F98_{BL}$ and DI TNC1 cells growing in a T-25 flask using the PureLink RNA Mini Kit (Ambion) according to the manufacturer protocol. In brief, 600 µl of Lysis Buffer was added evenly to the flask for five minutes before transferring the solution into an RNase-free tube. The solution was vortexed and homogenized by repeated passage through an 18-gauge needle using a 3 ml syringe. 600 µl ethanol was added and the solution vortexed before two subsamples of 605 µl were added to a spin column and centrifuged at 12,000 rcf for 15 seconds (the conditions for all centrifugations unless otherwise noted) serially in the same tube for a given cell line sample. 700 µl of one wash buffer was added and the solution centrifuged; twice, 500 µl of a distinct wash buffer was added and the solution centrifuged. The spin cartridge membrane was dried before 100 µl sterile, deionized (DI) water was added to the RNA which remained in the cartridge for one minute before centrifugation for 2 minutes at 13,000 rcf to collect the RNA sample, which was aliquoted and immediately stored at 193 K.

Upon thawing, the purity of the RNA was confirmed, and its concentration measured using a NanoDrop One (Thermo Fisher Scientific). 2.5 µg of RNA was incorporated into a 20 µl total volume composition, as prescribed and provided by the iScript Advanced cDNA Synthesis Kit for RT-PCR (Biorad), in order that each PCR well contain approximately 25 ng of cDNA. The

RNA was reverse transcribed, at optimal reverse transcriptase temperature (319K) for 20 min (Nexus Mastercycler, Eppendorf) before the reverse transcriptase was inactivated by heat for 1 min at 368K.

PCR was performed for each cell type in technical duplicates. A third replicate was forgone due to the low variability observed following two replicates. 19 µl of reaction mix (SsoAdvanced Universal SYBR Green Supermix, Biorad) was added to each well of the PCR plate (Ephrin Signaling R96 Plate, Biorad, modified to include wells with primers for rat EPH A5, EPH A6, EPH A7, IL-13, IL-13Rα2, IL-13Rα1, and IL-4Rα) in a BSC before 1 µl of cDNA (1% of the total volume of cDNA solution) was added to each well. The wells were sealed using optical strips (MicroAmp, Applied Biosystems), and the plate was vortexed and centrifuged (4,000 rpm, 2 min) to remove bubbles before colorimetric measurements in an ABI QuantStudio programmed to activate the reactions by bringing the plate to 368 K for 2 min, 40 cycles of denaturation (368 K, 5s) and annealing (333 K, 30 s), and a SYBR Green melt curve (338-368 K) to distinguish specific amplification. The presence of each gene of interest was evaluated on the basis of exponential amplification, as observed from the elongation graph and the basis of specificity, as observed from the melt curve graph, before ΔΔCT analysis was performed using the CT values from the QuantStudio software, using DI TNC1 as a reference sample and GAPDH as a reference gene. ΔCT values for genes were calculated for $F98_{BL}$ and DI TNC1 cells relative to each cell's GAPDH expression. ΔΔCT values for $F98_{BL}$ genes were calculated relative to the corresponding DI TNC1 ΔCT value for that gene.

Immunocytochemistry

$F98_{BL}$ and DI TNC1 cells were seeded at 20,000 cells per well in 24-well plates with a 12 mm glass coverslip and allowed to grow until they reached an appropriate confluency. Cells were

treated with a 1:1 mixture of 10% formalin (Fisher Chemical) and PBS for two minutes before being fixed in 10% formalin for 30 minutes, after which they were washed with PBS. Wells were split into three groups depending on treatment: Group 1 was stained with a mouse antibody for rat EPH A2 (Invitrogen) and subsequently a secondary Alexa Fluor 568-bound goat anti-mouse antibody (Invitrogen); Group 2 was a control that only was treated with the secondary antibody; and Group 3 received PBS when the others were exposed to antibodies. Wells in Groups 1 and 2 were further stained with either 4′,6-diamidino-2-phenylindole (DAPI) (Millipore Sigma) (1:5,000) and phalloidin bound to Alexa Fluor 488 (1:200) (Invitrogen), or DAPI alone. Cells in Group 3 were not stained. Washes were performed after each stain and antibody treatment stage. One drop of Fluoramount-G (Southern Biotech) was applied to 24 mm x 55 mm rectangular coverslips (Thermo Scientific). The 12 mm diameter circular coverslips were removed from the wells with fine-tipped tweezers, dried by pressing the edge against a Kimwipe (Kimberly-Clark Professional), and placed cell-side down onto the Fluoramount drop. The coverslips were left to sit overnight in a dark room before the edges of the circular coverslip were sealed onto the rectangular coverslip using clear nail polish and imaged at least 30 minutes later using a Zeiss LSM 800 confocal microscope.

Viability Assays

A calibration curve of absorbance at 490 nm was established for 0, 500, 1,000, 3,000, 7,500, 15,000, and 20,000 $F98_{BL}$ or DI TNC1 cells in quadruplicate using CellTiter 96 ® AQueous Cell Proliferation Assay (Promega), consisting of 2 mg/ml 3-(4,5-dimethylthiazol-2-yl)-5-(3-carboxymethoxyphenyl)-2-(4-sulfophenyl)-2H-tetrazolium, inner salt (MTS) and 3 mM phenazine methosulfate (PMS). From the calibration curve, a cell seeding number was selected that would allow for distinguishing initial seeding number intensity from background while

giving cells the opportunity to proliferate within the linear range below the point of live signal for a fully confluent well (between 15,000 and 20,000 cells). For $F98_{BL}$ cells, 5,000 cells per well were seeded into a 96-well plate and incubated for 24 hours. DI TNC1 cells were seeded at 8,500 cells/well. QUAD 3.1-WP396 was serially diluted in sterile, DI water such that identical volumes were added to 0.1% bovine serum albumin (Fischer Bioreagents) in PBS for final concentrations of 100 pM, 1,000 pM, 10,000 pM, or 100,000 pM. The same volume of digitonin (final concentration: 25 – 100 μg/ml) (Millipore Sigma) in sterile, DI water was diluted in 0.1% bovine serum albumin in PBS for a dead cell control, and the same volume of sterile, DI water was diluted in 0.1% bovine serum albumin in PBS for a live cell control. After incubation, the growth medium was aspirated off and replaced with 100 μl of the appropriate treatment solution, with 4 replicates per treatment for each cell line. The treated cells were incubated for an additional 48 hours ($F98_{BL}$) or 72 hours (DI TNC1) prior to the removal of the treatment solution, which was replaced with 100 μl of growth medium. Subsequently, 20 μl of 200:1 MTS:PMS was added to each well. They were then incubated for 75 minutes before the absorbance at 490 nm was measured using a SpectraMax M2 spectrophotometer. Data was normalized by subtracting from all signals measured, including live cell control, either a no-cell control with MTS and PMS (DI TNC1) or a dead-cell control with MTS and PMS ($F98_{BL}$) and dividing signal by the signal of the background-subtracted live cell control; standard deviation was normalized as the ratio of the raw standard deviation to the raw live cell control signal intensity. The Hill equation was used to determine the IC_{50} dose for QUAD-WP396 acting on $F98_{BL}$ viability.

Results

Gene Expression

Polymerase chain reaction assays were used to determine the transcription levels for genes relevant to QUAD-CTX treatment for both $F98_{BL}$ and DI TNC1 cells. GAPDH was used as a reference gene, so ΔCT values for each of the genes of interest are calculated relative to the CT for GAPDH within cell type. For gene expression in $F98_{BL}$ cells, the ΔΔCT value for a specific gene was calculated relative to the ΔCT value for that gene in DI TNC1 cells. Among the targets of QUAD-CTX, measured EPH A2 transcription levels were 2.18 times higher in F98BL cells relative to DI TNC1 cells, and measured EPH B2 transcription levels were 1.13 times higher (Table 3.1). EPH A3 was transcribed at low levels in DI TNC1 cells (CT ≈ 30, ΔCT ≈ 12; as expression levels decrease, CT values increase) but not detectable in F98BL cells. Neither cells had detectable mRNA levels coding for IL-13Rα2. The baseline transcription levels of the ligands themselves were also of interest to us: neither cells had detectable levels of IL-13 mRNA, while F98BL cells had 0.04 times the measured ephrin A5 mRNA levels as DI TNC1 cells. Ephrin A1 mRNA, on the other hand, was measured to be 5.66 times more prominent in F98BL cells. Other EPH targets of ephrin A5 were also probed: in F98BL cells, measured EPH A1 transcription levels were 0.55 times those of DI TNC1 cells, while measured EPH A5 levels were 1.28 times higher. Only detected in DI TNC1 cells was EPH A4 (CT ≈ 28; ΔCT ≈ 10) and EPH A7 (CT ≈ 32; ΔCT ≈ 14) mRNA. Neither cells showed observable transcription levels for EPH A6. Though QUAD-CTX uses IL-13.E13K, the lower affinity receptors IL-13Rα1 and IL-4Rα were also investigated; the former had F98BL transcription levels observed to be 1.30 times as high as the DI TNC1 levels, while the latter had 0.99 times the measured expression in F98BL cells compared to DI TNC1 cells. The near identical GAPDH CT values for the two samples

Table 3.1.

Gene	ΔCT ($F98_{BL}$)	ΔCT (DI TNC1)	ΔΔCT	Relative Expression Factor
EPH A2	6.94	8.07	-1.12	2.18
EPH A3	-	11.92	-	-
EPH B2	8.62	8.80	-0.18	1.13
IL-13Rα2	-	-	-	-
IL-13	-	-	-	-
Ephrin A1	9.78	5.20	4.58	5.66
Ephrin A5	7.43	9.93	-2.50	0.04
EPH A1	12.06	11.21	0.85	0.55
EPH A4	-	9.98	-	-
EPH A5	11.11	11.47	-0.35	1.28
EPH A6	-	-	-	-
EPH A7	-	13.98	-	-
IL-13Rα1	7.78	8.16	-0.38	1.30
IL-4Rα	9.12	9.10	0.02	0.99

(17.96 in F98BL, 17.98 in DI TNC1) and the theoretically identical RNA input between the two samples provides a justification for expressing the sum of the relevant ephrin A5 targets in terms of GAPDH expression. For DI TNC1 cells, RNA encoding the three primary EPH targets of QUAD (EPH A2, EPH A3, and EPH B2) was 6.2 * 10-3 the levels of GAPDH RNA, and all

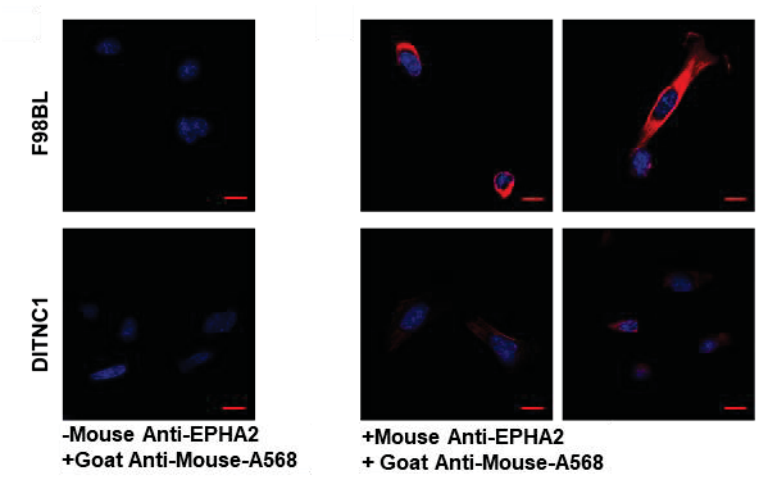

Figure 3.1. EPH A2 expression. $F98_{BL}$ cells were stained using a mouse anti-EPH A2 primary antibody and a goat anti-mouse secondary antibody bound to Alexa Fluor 568. Blue fluorescence indicates cell nuclei, while red fluorescence indicates the presence of EPH A2; the green fluorescent channel is excluded from the images presented. Both $F98_{BL}$ and DI TNC1 cells express EPH A2, though it is higher and more polarized in $F98_{BL}$ cells. Scale bar denotes 10 μm.

EPH targets of ephrin A5 (EPH A1, EPH A2, EPH A3, EPH A4, EPH A5, EPH A6, EPH A7, and EPH B2) had 8.1 * 10-3 the RNA levels of GAPDH. For F98BL cells, the relative RNA levels are 10.7 * 10-3 for the primary QUAD targets and 11.3 * 10-3 for all ephrin A5 receptors.

EPH A2 Localization

$F98_{BL}$ cells were shown to express EPH A2; however, so were DI TNC1 cells (Figure 3.1). F98 cells exhibited very dense EPH A2 expression that was near-ubiquitous across the cell surface. In many cases, it was observed to be particularly dense on a certain contiguous portion of the membrane, often comprising roughly one half of the membrane's perimeter in the x-y plane. The DI TNC1 cells more often showed a lower intensity signal dispersed across an often larger cell surface. The second experimental group (no primary antibody control) showed no red fluorescent

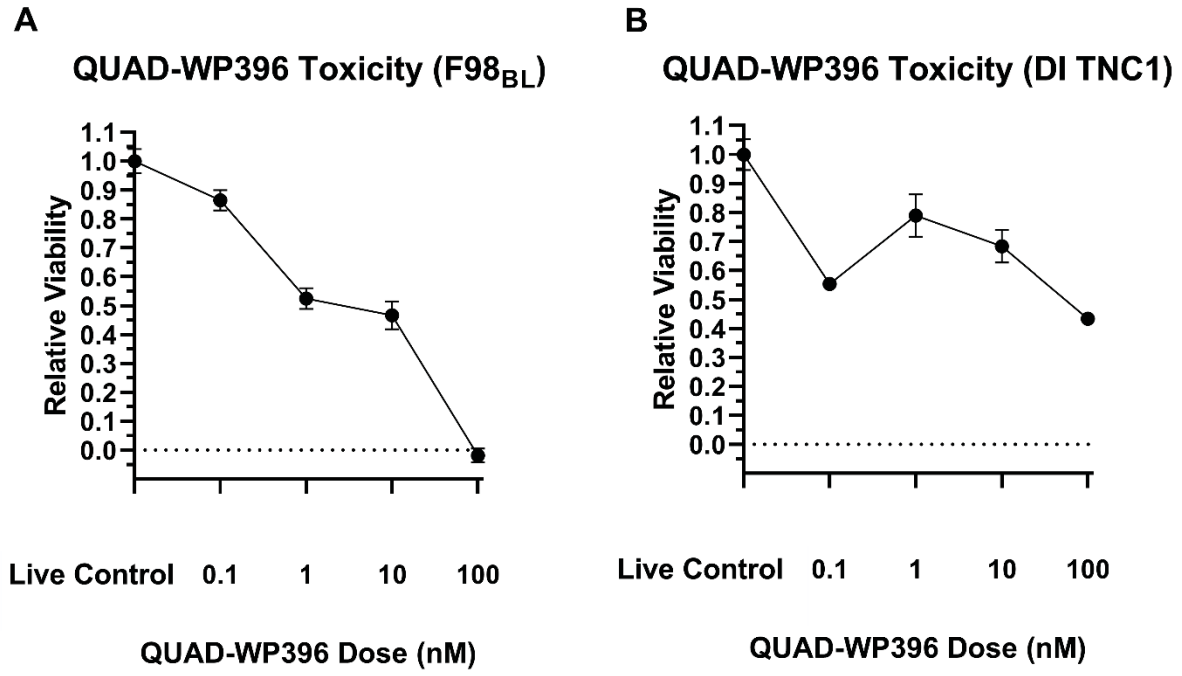

Figure 3.2. QUAD-WP396 toxicity. Cells were plated in quadruplicate and exposed to various concentrations of QUAD 3.1-WP396. Viability was normalized by subtracting background and dividing by QUAD 3.1-WP396-free live cell control signal; live cell control is shown on the axis. $F98_{BL}$ cells show decreased viability with increased QUAD 3.1-WP396 concentration; half of the cells are dead between 1,000 pM and 10,000 pM; all cells are dead at 100,000 pM (A). DI TNC1 cells, on the other hand, seemed to show no clear viability correlation with QUAD 3.1-WP396 (B).

signal, indicating no off-target antibody activity, and the third group had no identifiable fluorescence, indicating minimal autofluorescence, excepting $F98_{BL}$ GFP expression.

Effect of QUAD-WP396 on Viability

Initially both $F98_{BL}$ and DI TNC1 cells were tested by seeding at 5,000 cells/well in a 96-well plate, but it became apparent that DI TNC1 cells required different growth conditions and exhibited a different per-cell response to the live stain, so they were surveyed again using a modified protocol (see Methods) that involved seeding them at 8,500 cells/well. After adhesion

to the wells, cells were exposed to logarithmically varied doses of QUAD-WP396 in 0.1% BSA in PBS for 48-72 hours before viability was measured using an MTS assay. The observed average $F98_{BL}$ viability decreased with each successive increase in dose of QUAD-WP396 administered (Figure 3.2A). DI TNC1 mean viability remained fairly stable across all doses of QUAD-WP396 administered (Figure 3.2B). The IC_{50} for $F98_{BL}$ was calculated to be 2,348 pM.

Discussion

EPH A2 is more highly expressed on $F98_{BL}$ cells than DI TNC1 cells, by a factor calculated at 2.18. The levels of the other three receptors were comparable between the two cell types: $F98_{BL}$ expression of EPH B2 was slightly higher, DI TNC1 expression of EPH A3 was low while $F98_{BL}$ expression of it was undetectable, and neither cell line showed detectable levels of IL-13Rα2. The lack of detectable IL-13Rα2 and EPH A3 receptor expression in $F98_{BL}$ cells is not a significant setback to our tests of the efficacy of QUAD-CTX, as QUAD was designed to target four over-expressed receptors using a single therapeutic molecule. The overexpression of EPH A2 by $F98_{BL}$ cells provides an opportunity for QUAD-CTX to target $F98_{BL}$ cells.

Ephrin A5 levels were much lower for $F98_{BL}$ cells, with $F98_{BL}$ cells observed to transcribe only about 4% as much ephrin A5 as DI TNC1 cells; the ΔCT observed for ephrin A5 in DI TNC1 cells was lower than for any other QUAD-related molecule tested (5.20), indicating high ephrin A5 expression in DI TNC1 cells. This may be promising for both therapy and clarity of results in the *in vivo* model, as there will be relatively low ephrin A5 expressed endogenously by $F98_{BL}$ in competition with the functional ephrin A5 component of QUAD. As ephrin A5 expression is higher among DI TNC1 cells, this may result in fewer targets of ephrin A5, and therefore also of QUAD, unbound among healthy cells and more unbound QUAD targets in the tumor

environment. Interestingly, 5.66 times more ephrin A1 transcription was measured in $F98_{BL}$ cells compared to DI TNC1 cells. In human cells, neither healthy cells nor GBM cells expressed much ephrin A1[30]. The ΔCTs measured for ephrin A1 were lower than for most other molecules studied, indicating a higher rate of transcription (Table 3.1). However, these ΔCT values were not higher compared to other non-membrane bound proteins expressed (Table 3.1). It is possible that their presence as protein may not be relatively high if their destruction rate is also relatively high. Protein expression assays are needed for further clarity. The lack of IL-13 transcription by either cell type means there will be no endogenous interference with QUAD target receptors from this ligand. As there was no IL-13Rα2 transcription observed and levels of both IL-13Rα1 and IL-4Rα were comparable between cells, the functionality retained by QUAD's constituent ligands may be an interesting area of study. As previously mentioned, IL-13 binding to IL-13Rα1 and subsequent complexing with IL-4Rα leads to downstream apoptotic resistance pathways[36,37], which may complicate the action of the conjugated cytotoxin. However, the fact that the IL-13 constituent of QUAD, IL-13.E13K, has a reduced affinity for IL-13Rα1 may mitigate this concern.

All ephrin A5 receptors for which rat primers were available, EPH A1, EPH A2, EPH A3, EPH A4, EPH A5, EPH A6, EPH A7, and EPH B2, were compared as a whole. As GAPDH, the reference gene chosen for comparing all genes of interest, had a very similar CT value between the two cell types (17.96 vs 17.98), such an analysis seems particularly useful for comparison. This analysis was done by calculating for each of these genes the expression factor relative to GAPDH. In other words, instead of calculating the relative expression factor from the ΔΔCT value, it was calculated for the ΔCT of each gene of interest for each cell type relative to that cell's CT for GAPDH. These relative expression factors were summed for each cell. For $F98_{BL}$

cells, this sum of relative expression factors was $10.7 * 10^{-3}$ the level of GAPDH transcription, while for DI TNC1 cells, it was only $8.1 * 10^{-3}$ relative to GAPDH. When only the three targets that inspired the creation of QUAD, namely EPH A2, EPH A3, and EPH B2, were included in this analysis, the combined transcription levels of these targets was $11.3 * 10^{-3}$ that of GAPDH in $F98_{BL}$ cells and $6.2 * 10^{-3}$ that of GAPDH in DI TNC1 cells. The latter summation supports the effectiveness of QUAD selectivity on the basis of the intended targets, and the former suggests that off-target ephrin binding to other EPH receptors will not be a problem.

These results provided very useful context for transcription; however, we were also interested in protein expression. Transcription is a measure of the rate of addition of a protein, but other factors, such as rate of destruction and baseline prevalence, also influence the total amount of protein present on the cell surface, which is the paramount consideration in molecular targeted therapy. Therefore, we stained $F98_{BL}$ and DI TNC1 cells with a primary antibody targeting EPH A2 and a red fluorescent secondary antibody, allowing for visualization of EPH A2 for each cell type. This immunocytochemical staining shows that $F98_{BL}$ cells express EPH A2, which suggests that they should be targetable using QUAD. DI TNC1 cells also expressed EPH A2, a result which was not expected based on human EPH A2 expression patterns[51]. $F98_{BL}$ cells expressed much higher levels of EPH A2. They expressed it across their entire cell surface, whereas EPH A2 expression on DI TNC1 cells was limited to sparse networks. Furthermore, even when comparing the loci where each expressed EPH A2, the density of expression was much higher for $F98_{BL}$ cells, as indicated by saturation or near-saturation of red fluorescent signal and pixel width of EPH A2-positive areas. Given the omnipresence and density of EPH A2 on $F98_{BL}$ cell surface, QUAD binding seems very likely given any QUAD-$F98_{BL}$ contact.

Nevertheless, the presence of ephrin A5 receptors on DI TNC1 cells is undeniable, so off-target effects of QUAD-CTX on DI TNC1 cells are possible. To explore the effectiveness of a QUAD-conjugate to modified doxorubicin, we tested the viability of cells *in vitro* in response to varying doses of QUAD-WP396. Seeding, incubation, and background subtraction methods were adjusted between the two cell lines based on their growth and metabolic characteristics. The viability of $F98_{BL}$ cells decreases with increasing QUAD-WP396 dose (Figure 3.2A), from 86% viability at 100 pM to near-zero viability at 100,000 pM. The IC_{50} dose for QUAD-WP396 acting on $F98_{BL}$ was calculated to be 2.348 nM. This dose required for killing half of the $F98_{BL}$ population is comparable to the IC_{50} observed for various human GBM cells which fell between 1.1 nM and 3.1 nM[40]. The consistency between IC_{50} values for the various cell lines, even across multiple species of origin, suggests that the strategy underlying the development QUAD, to target GBM regardless of receptor profile, may prove successful, particularly in our model. No pattern between viability and dose is apparent for DI TNC1 cells (Figure 3.2B), with viability observed for all doses being between 43% and 79% of the live cell control signal. If there is no dose-dependency for DI TNC1 cells, representing bulk healthy tissue, but there is for $F98_{BL}$ cells, the implication is that QUAD-CTX may selectively target tumor cells, particularly in our model. As normalized $F98_{BL}$ viability measured at 100 nM was near-zero, but DI TNC1 cells had a measured viability of 43.3% relative to the live cell control, some treatment that induces an ultimate parenchymal concentration at or below 100 nM may be beneficial. Further treatment planning work will follow, as it appears that QUAD-WP396 effectively kills $F98_{BL}$ cells at relevant doses.

Chapter 4: Blood-Brain Barrier Response to High-Frequency Electroporation

This chapter is adapted from work that has been published in Cancers (Volume 11, Issue 12) by Melvin F. Lorenzo, Sean C. Thomas, Yukitaka Kani, Jonathan Hinckley, Matthew Lee, Joy Adler, Scott S. Verbridge, Fang-Chi Hsu, John L. Robertson, Rafael V. Davalos, and John H. Rossmeisl, Jr., under the title "Temporal Characterization of Blood–Brain Barrier Disruption with High-Frequency Electroporation"[52].

Introduction

While the other work conducted in this document focuses on the tumor component of the rat model, this work focuses on the host component. Of great importance to a combinatorial therapy is the question of whether one therapy enhances the effectiveness of the other. As QUAD-CTX has previously been delivered using convection-enhanced delivery[40], which bypasses the BBB using cannulae, one obvious way pulsed electric fields can enhance the effectiveness of QUAD-CTX is by blood-brain barrier disruption. BBBD has been achieved through traditional IRE waveforms[20,41,42]. Notably, BBBD results from exposure to weaker electric fields than irreversible electroporation and even reversible electroporation[41]. These findings recommend the prospect of using high-frequency pulsed electric fields to induce BBBD that is useful for treatments.

In this chapter, we apply high-frequency electroporation (HFE), distinct from H-FIRE, high-frequency irreversible electroporation, as its intended purpose is not to ablate tissue to the point of irreversible electroporation and cell death, to the brains of Fischer rats. Besides establishing

BBBD by HFE, we were also interested in the duration of potential BBB disruptive effects; such knowledge would aid greatly in treatment planning. Individual rats were assigned to groups designated to have their BBBD studied at different timepoints following HFE. Blood-brain barrier disruption volume (BBBDV) was quantified by injecting markers that are typically BBB-impermeable and measuring the volume of brain parenchyma into which they had penetrated.

Methods

Rodent Handling and HFE Application

Male Fischer rats were inspected twice daily for adequate food consumption, responsiveness, and alertness, both following treatment and during the acclimation phase lasting for one to two weeks prior to treatment. Immediately preceding treatment, the subjects were injected with 1 mg/kg buprenorphine (Buprenoprhine SR-LAB, Zoopharm) and anesthetized with isoflurane (3-4%:95 isoflurane:oxygen mixture) until non-responsive to minor pain stimulus (paw squeeze). Their heads were shaved, their eyes were lubricated, and their anesthetization was maintained using isoflurane (2-3.5%:95% isoflurane:oxygen) delivered via nosecone. A Dremel drill with a round bit was used to create a defect in the cranium and a scalpel used to part the dura mater before rostral electrode insertion 4 mm caudal to the bregma, 3.5 mm lateral to the bregma. Two electrodes with 0.45 mm diameter and 1 mm exposure length, separated by 4 mm center-to-center, were inserted 4 mm below the dura mater. Under sham conditions, no pulses were applied as the electrodes remained inserted for slightly more than 200 seconds. In other cases, various pulse parameters were applied, all of which entailed high-frequency pulses delivered in a 5-5-5 scheme with 1 Hz bursts and 100 μs energized time per burst, as further detailed in the treatment matrix (Table 4.1). A custom-crafted EPULSUS-FBM1-5 generator[53] was used to deliver a pulse

Table 4.1.

Group	Time Point (h)	V/d Ratio (V/cm)	Burst Number	Replicates	Replicates for Pathological BBBD Analysis
Sham	1	0	0	2	2
1-hour	1	600	200	4	3
24-hour	24	600	200	8	7
48-hour	48	600	200	8	8
72-hour	72	600	200	8	8
96-hour	96	600	200	4	4
H-FIRE	1	1200	200	4	4
$Burst_{100}$	1	600	100	4	4

scheme programmed by UCB-06 software. Once pulsing was ceased, the electrodes were removed. The breach in the cranium was bridged with bone wax (Ethicon) before suturing resealed the integumentary boundary.

Blood-Brain Barrier Disruption Volume Quantification

At the previously determined timepoint following the application of pulses (Table 4.1), an intraperitoneal injection was administered containing 75 mg/kg 2.5% Evans Blue Dye (EBD) (Millipore Sigma) and 100 μmol/kg gadopentetate dimeglumine (Gd) (Magnevist, Bayer)

contrast agent for magnetic resonance imaging (MRI). Animals were euthanized using 500 µl pentobarbitol (Fatal Plus, Vortech Pharm).

Penetration of Gd into the brain parenchyma was measured using T1W-weighted MRI contrast (Philips 1.5 T scanner with 8-channel head coil, Intera, Philips Healthcare; TR = 450 ms, TE = 15 ms, FOV = $(40\ mm)^2$); slice thickness was 2 mm. Osirix (Osirix MD) was used to create and quantify 3D reconstructions from these image slices.

To quantify Evans Blue Dye penetration into brain tissue, gross pathological analysis of 10 µm tissue sections at 200 µm intervals was conducted. A CCD camera (Nikon DS-Fi1c, Nikon) collected digital photomicrographs (Nikon Eclipse Ni-E, Nikon) to determine the area where EBD was present in each tissue section. 3D Slicer 4.10 software (Slicer) was used to create quantifiable volumes from these measurements.

Effects of Energy Application

Pilot studies were conducted to determine optimal HFE pulse parameters for BBBD, comparing different strategies of energy application. For a 5-5-5, 1 Hz, 100 µs on-time/burst HFE configuration, burst number (0, 100, and 200) and the ratio of pulse voltage to electrode distance (V/d ratio) (0, 600, and 1200 V/cm) were manipulated (Table 4.1). Subsequently, BBBDV was measured by gross pathological analysis.

Temporal Characterization of Blood-Brain Barrier Disruption

In accord with the procedures described above, HFE with the following characteristics was applied: 5-5-5, 1 Hz, 200 bursts, 100 µs energized time/burst, and 600 V/cm V/d ratio. Animals were injected with BBB-impermeable markers at the following timepoints: 1 hour, 24 hours, 48

hours, 72 hours, and 96 hours, following treatment (Table 4.1). The BBBDV was quantified using analyses of both gross pathology and T1W-weighted MRI scans.

Computation of Electric Field Threshold Required for Blood-Brain Barrier Disruption

Electric field thresholds were determined in the following manner. Blood-brain barrier disruption volumes were reconstructed from EBD area in tissue sections and quantified using 3D Slicer 4.10. In brief, the electric field distribution throughout the brain was modeled using COMSOL Multiphysics v5.4 (COMSOL Inc.) given the electrical properties of the tissue and the pulse parameters. The electric field magnitude for which field lines enclosed the volume equivalent to the BBBDV was determined to be the EFT required for BBBD.

Results

Effects of Energy Application

We began by studying responses to differences in energy application. For a 5-5-5, 1 Hz, 100 μs on-time per burst, 600 V/cm V/d ratio treatment, groups received the application of 0 (sham), 100, or 200 bursts and had Gd-EBD injected one hour after pulsing. The BBBDV values for these groups were 0.0 ± 0.0 mm^3, 87.0 ± 5.6 mm^3, and 81.2 ± 7.9 mm^3, respectively (Figure 4.1A). A significant difference was detected among all three groups (Kruskal-Wallis, $p < 0.05$), but post-hoc comparison found no significant differences between any specific set of two groups, whether it be 0 versus 100 bursts (post-hoc Dunn's test, $p = 0.06$), 0 versus 200 bursts ($p = 0.61$), or 100 versus 200 bursts ($p = 0.79$).

In addition to the treatment duration, the pulse magnitude was also tested. For a 5-5-5, 1 Hz, 200 bursts, 100 μs on-time per burst treatment, the V/d ratio applied was varied between 0 V/cm

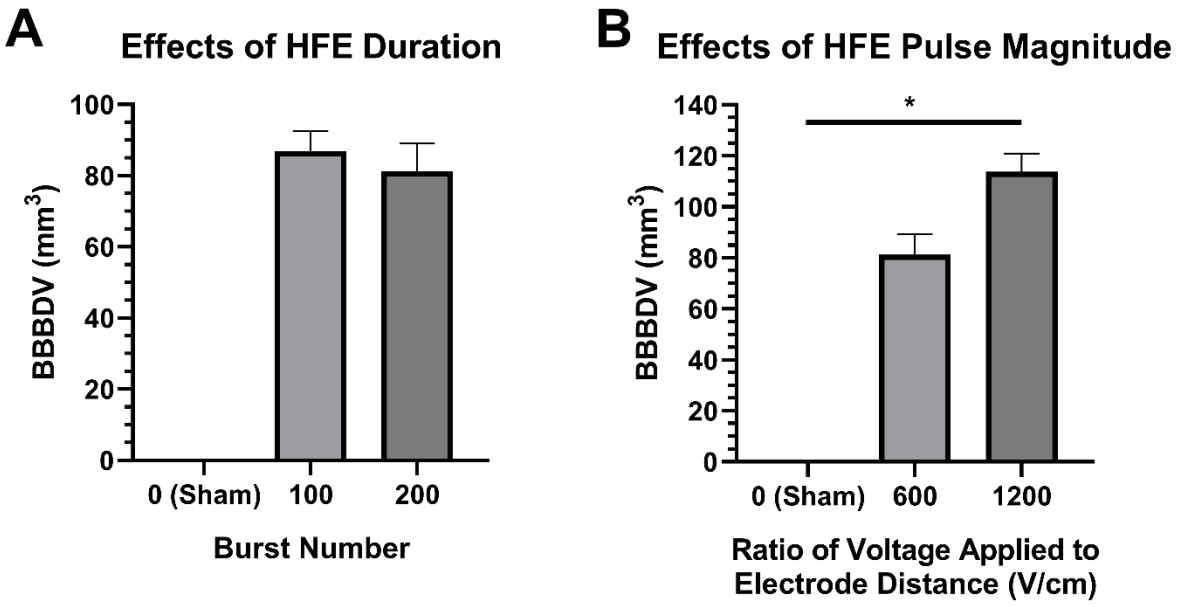

Figure 4.1. Blood-brain barrier disruption volume in response to 2-fold manipulations in energy delivery. Rats were administered sham treatments with electrode insertion but no pulses delivered and an HFE treatment with the following parameters: 5-5-5, 1 Hz bursts, 200 bursts, 100 μs energized time per burst, 600 V/cm ratio of applied pulse voltage to electrode spacing distance (V/d ratio). When the effects of these pulse parameters were compared to the delivery of 100 bursts (A), all else held equal, no significant differences in mean were detected between any two particular groups. When the effects of the former pulse parameters were compared to the application of a 1,200 V/d ratio (H-FIRE group) (B), the increased energy application resulted in significantly differences among the three groups, particularly between the H-FIRE treatment and sham groups ($p < 0.05$).

(sham), 600 V/cm, and 1,200 V/cm. The mean BBBDV values for these groups were 0.0 ± 0.0 mm^3, 81.2 ± 7.9 mm^3, and 113.8 ± 7.1 mm^3, respectively (Figure 4.1B). At least one group's mean BBBDV was detected to be different from another's (Kruskal-Wallis, $p < 0.005$), with post-hoc comparisons revealing a significant difference between sham and H-FIRE (1,200 V/cm group) (post-hoc Dunn's test, $p < 0.05$).

Temporal Characterization of Blood-Brain Barrier Disruption

The temporal nature of BBBD mediated by HFE was studied by applying 5-5-5, 200, 1 Hz bursts with 100 μs of energized time at a V/d ratio of 600 V/cm and intraperitoneally injecting BBB-impermeable markers, EBD and Gd, 1, 24, 48, 72, or 96 hours later to quantify the volume of the brain parenchyma where BBBD was induced. BBBD volumes from gross pathological analysis

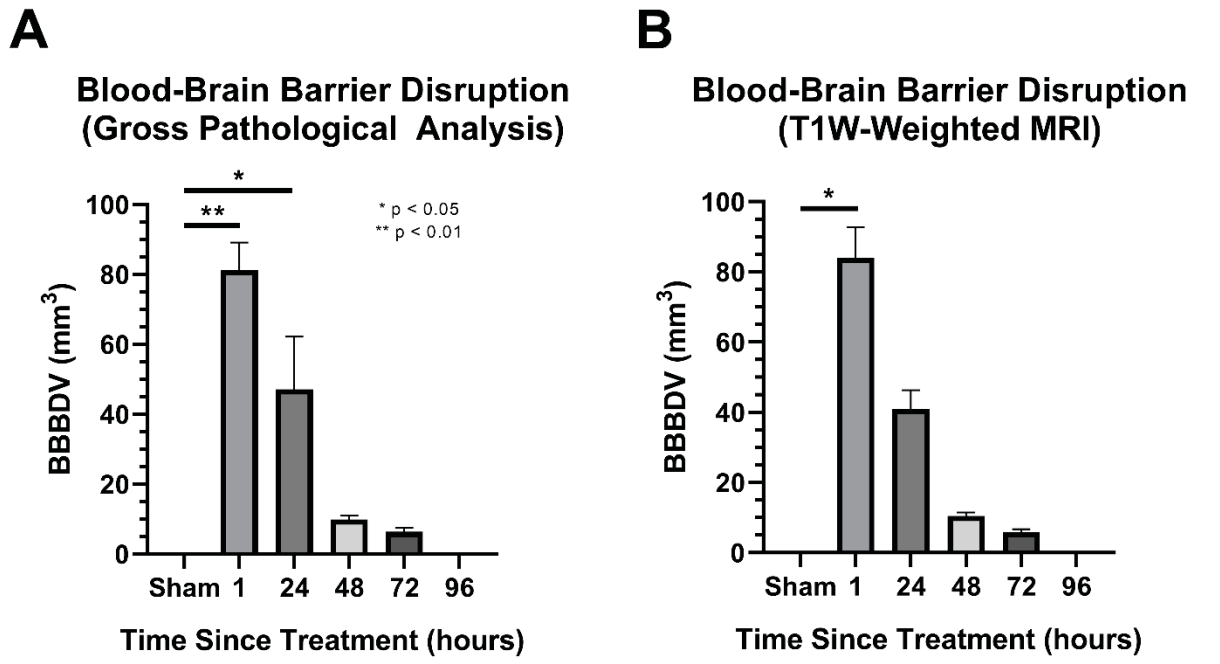

Figure 4.2. Blood-brain barrier disruption volume measured at various timepoints following HFE treatment. BBBDV was measured either by Evans Blue Dye presence in gross tissue sections (A) or by gadopentate dimeglumine contrast in T1W-weighted MRI (B). For the sake of visual simplicity, all post-hoc comparisons displayed are Dunn's tests in reference to the sham control. Both approaches of BBBDV measurement show no BBBD in sham treatments, with BBBDV decreasing from 1 hour to 72 hours following treatment, until no BBBD is observed after 96 hours.

were found to be greatest in the 1 hour group (81.2 ± 7.9 mm^3), with measured BBBDV decreasing for each successive group, from 24 hours (47.1 ± 15.1 mm^3) to 48 hours (10.4 ± 1.1 mm^3) to 72 hours (5.8 ± 1.0 mm^3) to 96 hours (0.0 ± 0.0 mm^3) (Figure 4.2A). At least one treatment group was detected to have a different mean BBBD volume (Kruskal-Wallis test, $p < 0.0001$); specifically, based on post-hoc comparison between all treatment groups, BBBD volumes measured for the 1-hour and 24-hour post-HFE injection groups were significantly different from the volume after 72 (post-hoc Dunn's, $p < 0.05$) or 96 hours ($p < 0.005$), as well as the volume in the sham treatment ($p < 0.05$). As measured by T1W-weighted MRI scans (Figure 4.2B), at least one group was detected to have a different mean from the others (Kruskal-Wallis

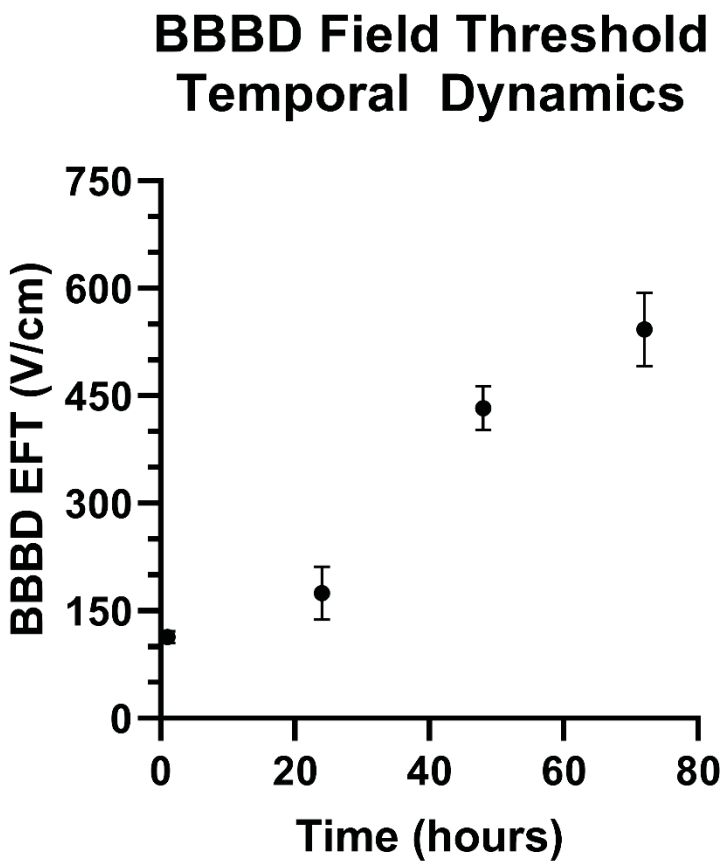

Figure 4.3. The electric field thresholds required to induce local blood-brain barrier disruption for various lengths of time. These were computed using numerical modeling based on BBBDV inputs from gross pathological analysis. Higher local pulsed electric field magnitude is required to induce BBBD for longer durations.

test, $p < 0.01$); with post-hoc comparisons to sham control, we found the BBBDV one hour following treatment to be significantly different from the volume observed in sham animals (post-hoc Dunn's test, $p < 0.05$). No statistically significant differences were found between the results of the two volumetric analysis methods for treatment groups (paired t-test, $p = 0.8357$).

Electric Field Thresholds Required for Blood-Brain Barrier Disruption

The EFTs required to induce BBBD were calculated from BBBDV values obtained from gross pathological analysis using COMSOL field distribution models. Lower EFTs were required to induce BBBD for shorter periods of time, with the EFT for disrupting BBB for 1 and 24 hours

computed to be 113.5 ± 8.2 V/cm and 174.9 ± 37.1 V/cm, respectively (Figure 4.3). Groups with greater delays before observation had higher numerically determined thresholds: 432.7 ± 30.8 V/cm for 48 hours and 542.5 ± 51.5 V/cm for 72 hours. The 96-hour group had insufficient blood-brain barrier disruption for quantifiable threshold calculation. The EFT required for local BBBD after 72 hours is significantly different from that required for hour-long and day-long BBBD ($p < 0.001$).

Discussion

There appears to be no difference in BBBDV observed at 1 h post-HFE between any particular pair of burst treatments, which include the sham, 100-burst treatment, and 200-burst treatment. A statistically significant difference was detected between means of the 0-burst, 100-burst, and 200-burst treatments, but post-hoc tests could not find a statistically significant difference between any two particular treatments. There was no difference detected in BBBDV for rats treated with 100 bursts versus 200 bursts. Though the statistical analysis does not explicitly support such an assessment, it does seem that there is a difference between BBBDV in rats that have been treated with HFE and rats that have not. The power of the statistical tests we used is limited by the small sample sizes, particularly of the sham treatment ($n = 2$). Following the first two replicates, as pathological BBBDV quantification revealed no quantifiable brain parenchymal tissue volume which EBD had stained, it was clear that there was no BBBD in sham-treated rats and that additional rodent subjects, which would have needed to be euthanized following treatment, would not be needed to support this assessment.

Differences in energy application were also tested with respect to pulse amplitude. 600 V/cm was the standard V/d ratio applied throughout this study. This was compared to sham treatment

(0 V/cm) and an ablative treatment, which used a V/d ratio of 1,200 V/cm. A statistically significant difference was detected between at least two of the three groups. Post-hoc tests found the H-FIRE (1,200 V/cm) treatment to result in a significantly higher BBBDV than the sham treatment. No significant differences could be detected by post-hoc tests between the HFE treatment and another group. Again, this may be the result of limitations of the power of our statistical analysis. Nevertheless, it can be concluded that differences in the amplitude of pulses applied have an effect on the volume of brain tissue in which the blood-brain barrier is disrupted.

When BBBD was evaluated at 1 hour, 24 hours, 48 hours, 72 hours, and 96 hours following HFE treatment, the volume of tissue where the BBB was disrupted decayed exponentially. Accordingly, BBBDVs measured by EBD penetration 1 hour and 24 hours post-HFE were significantly different from those measured at 72 hours and 96 hours post-HFE, as well as from sham-treated subjects. By 96 hours following HFE, the BBB had completely recovered, at least to the degree required to exclude EBD (~67.5 kDa, following complex formation with albumin) and Gd (560 Da). The geometry of BBB resolution is such that the first loci where subjects regain BBB integrity is the most distal area of initial BBBD, with BBBD lasting longest nearest the site of HFE application. This has important implications for treatment planning. HFE may be followed with repeated injection of QUAD-CTX or even standard chemotherapeutic agents. In cases wherein the electrodes are near the tumor centroid and the tumor geometry is not exceedingly irregular, this will generally result in loci with greater likelihood of surviving tumor cells receiving higher doses.

The two methods of evaluating BBBDV, gross pathological analysis and T1W-weighted MRI scans, produced notably similar results, with no significant differences found at any timepoint, despite differences in slice thickness and molecular size of BBB-impenetrable markers. The

molecular size of these markers must be considered when considering these results. The molecular weight of Gd is 560 Da, making it slightly larger than doxorubicin. The molecular weight of EBD is not much larger, at 960 Da; however, upon its addition to the bloodstream, it forms complexes with albumin. These complexes are much larger, approximately 67.5 kDa. The fact that no difference in BBBDV is detectable between volumetric quantification methods suggests that the process of BBB reformation post-HFE is such that at the point when 67.5 kDa molecules are locally excluded, so too are 560 Da molecules. The molecular weight of QUAD is approximately 72.5 kDa, and QUAD-WP396 has a molecular weight of approximately 73.5 kDa, both of which are comparable to EBD-albumin. QUAD-CTX is slightly larger than the EBD-albumin complex, indicating a low likelihood that local brain exclusion molecular size threshold differs between the two. Considering that the destructive nature of the mechanics of BBBD likely results in non-uniform size of BBB breach apertures, if there is no difference in BBBDV for ~600 Da and ~60,000 Da molecules, then an additional 6,000 Da seems unlikely to cause a molecule to exceed the BBB exclusion threshold.

The volumes of parenchyma that experienced BBBD at various timepoints were matched to the volumes enclosed by computationally modeled electric field contours to calculate EFTs required for BBBD at each successive time point post-HFE. Just as BBBDV decreased with increasing temporal separation from treatment, the EFT required for local BBBD increased with increasing temporal separation from treatment. The EFTs required for local BBBD at 1 hour and at 24 hours were significantly different from the EFT for BBBD 72 hours after treatment. Though there are only four time points for which EFTs for BBBD could be calculated, this increase appears to follow a sigmoidal pattern with a transitional phase centered on 40 hours. If EFTs for BBBD follow a sigmoidal pattern, then this may have useful implications for treatment planning. If the

space just beyond the tumor margin where tumor cells may have infiltrated is exposed to electric fields whose magnitudes are higher than the steep transition portion of the curve, then they may have greater exposure to a BBB-impermeable agent that selectively targets GBM cells.

Chapter 5: Effectiveness of High-Frequency Irreversible Electroporation Ablation of $F98_{BL}$ Cells

Introduction

In this chapter, we seek to determine whether H-FIRE selectively targets the tumor component of our model relative to DI TNC1 astrocytic cells, as it does human GBM cells relative to normal human astrocytes[27,28].

I also seek to answer the question fundamental to a combinatorial therapy, namely whether one therapy, QUAD-CTX, enhances the effectiveness of H-FIRE. As the ephrin ligands on QUAD retain their binding properties and receptor activating potential[40], I compared lethal H-FIRE thresholds for $F98_{BL}$ and DI TNC1 cells in response to ephrin A1 and ephrin A5.

Given the expression of some but not all QUAD targets by our tumor model cells, we were also interested in how ephrin would alter $F98_{BL}$ morphology, as there has been some speculation that the mechanism underlying increased H-FIRE selectivity in response to ephrin may be mediated by morphological changes[27,29].

Methods

Cell Culture

$F98_{BL}$ cells (developed from F98 cells, ATCC) and DI TNC1 *rattus norveticus* phenotype 1 astrocytes (ATCC) were cultured in Dulbecco's Modified Eagle's Medium (ATCC) with 100 units/ml penicillin, 100 µg/ml streptomycin (Gibco), and 10% added fetal bovine serum (Tissue

Cultures Biological 101). Cells were passaged when observed to be at 70% or higher confluency, or roughly every 48 hours for DI TNC1 cells and every 60 hours for F98 cells. DI TNC1 cells were passaged by removing the media, washing with 0.25% Trypsin-EDTA (Quality Biological), then incubating in 2 ml 0.25% Trypsin-EDTA for five minutes before neutralization with 6 ml media and seeding at a 1:6 dilution. $F98_{BL}$ cells were passaged by removing the media, washing with 0.05% Trypsin-EDTA (Gibco), then incubating in 2 ml 0.05% Trypsin-EDTA for five minutes before neutralization with 6 ml media and seeding at a 1:10 dilution.

Hydrogel Construction

Cells were seeded into 5 mg/ml collagen type I hydrogels at 1,000,000 cells/ml. The balance of components in these hydrogels is determined as follows: the dilution requirements for the final concentration of 5 mg/ml collagen determines the volume of stock collagen, dissolved in 0.1% acetic acid (Millipore Sigma), to add. This is supplemented by a mixture consisting of 1 N NaOH (Acros Organics), the volume of which is approximately 2.1% of the volume of stock collagen used, and 10X Dulbecco's Modified Eagle's Medium, the volume of which is 10% of the final volume of the gel solution. The remainder of the gel volume comes from the appropriate number of cells in growth medium. These hydrogels were plated into polydimethylsiloxane (PDMS) (Sylgard 184, Krayden) molds, previously sterilized and treated with sterile 1% polyethylimine (Acros Organics) in deionized water and sterile 0.1% glutaraldehyde (Fisher Bioreagents) in deionized water, capped with sterilized PDMS caps for thirty minutes following plating, and incubated at 310 K, shaping the hydrogels into cylinders with a 10 mm diameter and a depth of 1 mm. Subsequently, the caps were removed and 500 μl of media was added to the wells containing the mold and gels. Gels were incubated at 310 K, 5% CO_2 for 24 hours before treatment, the same conditions as all subsequent incubations.

Ephrin Treatment

As 100 μg/ml ephrin (Millipore Sigma) stock solution was constituted in sterile deionized water, a solution of more concentrated growth medium (for example, 1.0101X, 1.0309X, or 1.1111X growth medium for a 1:100, 3:100, or 1:10 dilution, respectively) was created for ephrin dilution. In experiments wherein treatment with ephrin was a component, the media was removed with a 2 ml plastic aspirating pipette (Cole-Parmer) 24 hours following gel creation and replaced with 1 μg/ml ephrin A1 or 1 μg/ml ephrin A5 in media. Then, cells were incubated for 12 h before pulsing.

H-FIRE Treatment

Before H-FIRE pulsing, medium was aspirated off the top of the gels and two stainless steel electrodes, formed out of 0.87 mm diameter needles (20 Gauge IT Series Blunt Stainless Steel Needle, Jensen Global) spaced 4 μm apart (center-to-center) were inserted into the hydrogel and held in place using a 3D printed 24-well plate well plug. Either a custom-crafted EPULSUS-FBM1-5 generator[53] or, in some cases, an H-FIRE 1.0 generator (Voltmed Incorporated), was used to deliver pulses. Growth medium was added immediately following pulsing. The hydrogels were then incubated for an additional 24 hours.

Threshold Quantification

The growth medium was removed from atop the gels and replaced with PBS containing propidium iodide dead cell red fluorescent stain (Millipore Sigma) and calcein green AM live cell green fluorescent stain (Calcein Green AM for Flow Cytometry, Invitrogen), and the well plate was incubated for 30 minutes. After 30 minutes, the staining solution was removed, and gels were washed in 600 μl PBS before being stored in 600 μl PBS until the time came for their

respective batch of 6-12 gels to be imaged. A 24-well plate lid was inverted and 30 µl PBS was added to the position on the lid where gels were to be placed for imaging. The PBS was removed from gels before 30 µl PBS was added to the top of the gels. The PDMS molds were removed from the well plates by fine-tip tweezers and placed gel-side down on the 30 µl drops on the 24-well plate lid. The small PBS volumes on the lid and gels primarily prevent discontinuities in the gel bodies from uneven placement or pieces of the gel falling, both of which are detrimental to whole-gel imaging, and secondarily maintain proper hydration of the gel throughout the duration of the imaging process. The well plate lid was placed on the adjustable well plate stage adaptor, which was tightened to fit the lid, and 88-tile, 10.8 mm total diameter circular geometry tile scans were taken of each hydrogel in the A555 (red fluorescent) and GFP (green fluorescent) channels using a 5X objective on a Zeiss LSM880 confocal microscope in the plane where the most cells were visible. The area where propidium iodide-positive cells were prevalent was measured using the spline graphics tool in ZEN Blue imaging software (Zeiss). The areas measured were inserted into a MATLAB (Mathworks) script that used a sixth-degree polynomial to fit a curve generated in COMSOL relating lesion area to the electric field magnitude enclosing an equivalent area given the pulsing parameters that were delivered to the hydrogels, as well as conductivity and other characteristics of the hydrogel model[54]. The MATLAB script (see Appendix A) would return the field strength whose isoline encompassed that same area, thus providing an approximate value of the lethal electric field threshold for a given cell line under given experimental conditions.

Pulse Schemes Studied

Lethal H-FIRE EFT studies used all of the methods described above, applying various waveforms at 750 V, 4 mm electrode separation, 50 bursts, 100 µs on time/burst, 1 Hz burst

frequency. Waveforms applied included 1-1-1, 1-2-1, 1-5-1, 2-1-2, 2-2-2, 2-5-2, 5-1-5, 5-2-5, 5-5-5, and 10-1-10. For each pulse scheme, pulses were applied using a mix of the EPULSUS-FBM1-5 generator[53] and the H-FIRE 1.0 generator.

For ephrin treatment, the pulses delivered used the following parameters: 1-5-1 pulse scheme, 750 V, 4 mm electrode separation, 100 bursts, 100 μs on time/burst, 1 Hz burst frequency. All pulses were applied using the EPULSUS-FBM1-5 generator[53].

Morphological Response to Ephrin

$F98_{BL}$ and DI TNC1 cells were plated in a 24-well plate with a 12 mm diameter coverslip lying in the well. 100 μg/ml ephrin A1 and ephrin A5 stock in sterile, DI water was diluted into sterile, pH-adjusted 1.0101X, 1.0309X, or 1.1111X DMEM to create 1 μg/ml, 3 μg/ml, and 10 μg/ml solutions of ephrin A1 and ephrin A5 in sterile medium. Cells in wells were pre-fixed with a 1:1 mixture of 10% formalin (Fisher Chemical) and PBS for 2 minutes and then fixed in 10% formalin for 30 minutes. They were washed three times with 500 μl PBS, then stained in 1:200 phalloidin-Alexa Fluor 555 (Cell Signaling Technology) and 1:5000 DAPI (Millipore Sigma) in 300 μl PBS at 310 K for 90 minutes. The staining solution was removed, and cells were washed three times with 500 μl PBS before storage in 300 μl PBS. One drop of Fluoramount-G (Southern Biotech) was added to a 24 mm x 55 mm rectangular coverslip (Thermo Scientific). The circular cover slips holding fixed cells were removed from the 24-well plate using fine-tipped tweezers and wicked by touching the edge of the face to a KimWipe (Kimberly-Clark Professional) before lightly placing the cell side onto the Fluoramount drop. These were left in a darkroom overnight before using clear nail polish to seal the two coverslips together to ensure no substrate shearing or fluid loss would take place. After the nail polish was allowed at least 30 minutes to dry completely, confocal microscopy images (Zeiss LSM880 confocal microscope)

were taken in z-stacks, in a range that included one step size beyond the most extreme z value at which phalloidin-A555 signal was observed for any cells, including cells not wholly within the field of view.

Each z-stack was opened in ImageJ, where it was split into a red channel and a blue channel. Each was converted to an 8-bit image before being saved as a PNG image sequence. These were loaded into 3D Slicer software (Slicer 4.10.2, Slicer), where the Image Spacing was entered appropriately (x: 0.0990358 μm; y: 0.0990358 μm; z: 1 μm) and the volume converted. The scalar volume was resampled as a 1, 1, 0.5-spaced b-spline to create a new scalar volume. Thresholds were set to include the lowest non-background pixel intensity, and each cell and nucleus, whole or partial, was highlighted distinctly in the plane at which the cells were densest and widest, the locus of a cell's highest z signal, the locus of a cell's lowest z-signal, at roughly 1 μm increments between those three z values, and at any z value where cells were growing too closely to entrust their differentiation to an algorithm. Each volume was then grown from those seeds (Figure 5.3A). Volumes were then quantified for each whole or partial cell or nucleus. Nucleus-to-cytoplasm ratios, nucleus-to-cell ratios, nucleus size, and cell size were all computed and statistically compared for F98 cells treated with 10 μg/ml ephrin A5 versus an ephrin-free control.

Results

High-Frequency Irreversible Electroporation Lethal Electric Field Thresholds

Lethal threshold experiments for H-FIRE treatments with the parameters 1 Hz bursts, 50 bursts, 100 μs on-time/burst, and 750 V, was conducted for various pulse schemes. For a 1-1-1 burst scheme, the lethal EFT for $F98_{BL}$ cells (n = 5) was 1,334 ± 350 V/cm, which was not

significantly different from the lethal EFT for DI TNC1 cells (n = 5), 1,710 ± 167 V/cm (Figure 5.1A). For a 1-2-1 burst scheme, the lethal EFT for $F98_{BL}$ cells (n = 5) was 1,451 ± 114 V/cm, which was not significantly different from the lethal EFT for DI TNC1 cells (n = 5), 1,535 ± 89 V/cm (Figure 5.1B). For a 1-5-1 burst scheme, the lethal EFT for $F98_{BL}$ cells (n = 5) was 1,190 ± 267 V/cm, while the lethal EFT for DI TNC1 cells (n = 5) was 1,631 ± 273 V/cm (Figure 5.1C). The lethal EFTs for the 1-5-1 pulse scheme were significantly different between healthy and

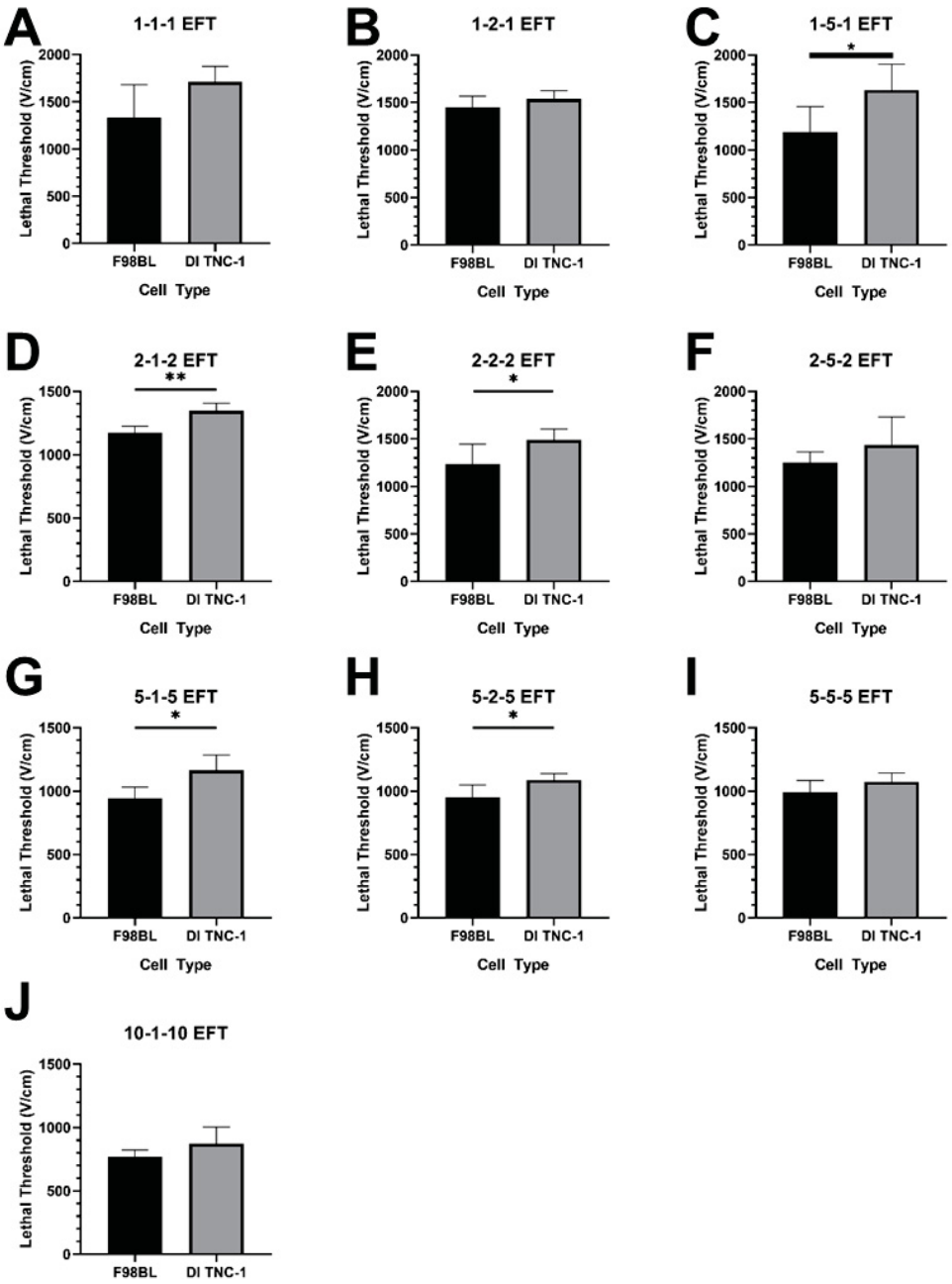

Figure 5.1. Lethal H-FIRE EFTs. F98BL and DI TNC1 cells were seeded into hydrogels and pulsed with H-FIRE (50 bursts, 1 Hz, 100 μs on-time, 750 V). The H-FIRE pulse scheme was varied. Lethal EFTs were calculated for each pulse scheme. $F98_{BL}$ lethal EFTs were significantly lower than DI TNC1 lethal EFTs for the 1-5-1 (C), 2-2-2 (E), 5-1-5 (G), 5-2-5 (H) ($p < 0.05$), and 2-1-2 (D) ($p < 0.005$) pulse schemes. No significant differences between $F98_{BL}$ and DI TNC1 cells was found for 1-1-1 (A), 1-2-1 (B), 2-5-2 (F), 5-5-5 (I), or 10-1-10 (J) schemes.

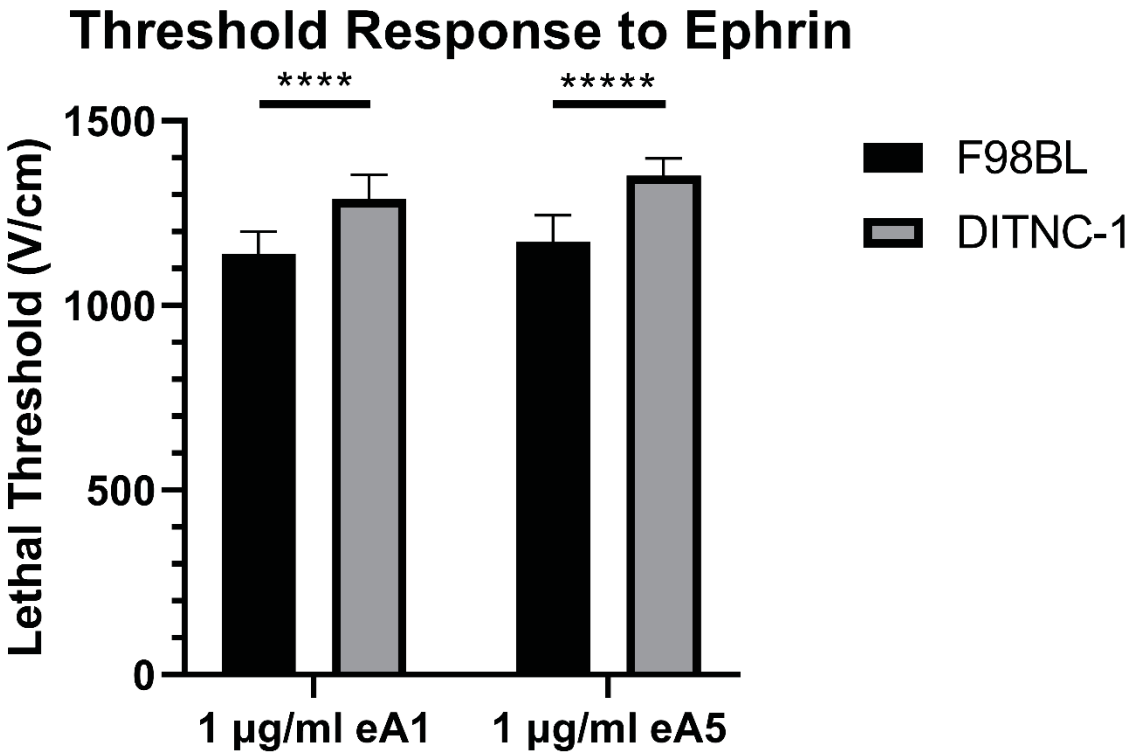

Figure 5.2. Lethal H-FIRE EFTs following exposure to ephrin. $F98_{BL}$ and DI TNC1 cells were seeded into hydrogels. Their media was changed 24 hours later to include either 1 µg/ml ephrin A1 or 1 µg/ml ephrin A5. Following 12 hours of incubation in ephrin, they were treated with H-FIRE using the following parameters: 1-5-1, 750 V, 1 Hz bursts, 100 bursts, 100 µs on-time per burst. $F98_{BL}$ cells had significantly lower thresholds than DI TNC1 cells under both ephrin treatments (ephrin A1: $p = 0.0001$; ephrin A5: $p < 0.0001$).

malignant cells ($p < 0.05$). For a 2-1-2 burst scheme, the lethal EFT for $F98_{BL}$ cells ($n = 5$) was 1,172 ± 55 V/cm, while the lethal EFT for DI TNC1 cells ($n = 5$) was 1,345 ± 58 V/cm (Figure 5.1D). The lethal EFTs for the 2-1-2 pulse scheme were significantly different between healthy and malignant cells ($p < 0.005$). For a 2-2-2 burst scheme, the lethal EFT for $F98_{BL}$ cells ($n = 5$) was 1,236 ± 211 V/cm, while the lethal EFT for DI TNC1 cells ($n = 5$) was 1,489 ± 114 V/cm (Figure 5.1E). The lethal EFTs for the 2-2-2 pulse scheme were significantly different between

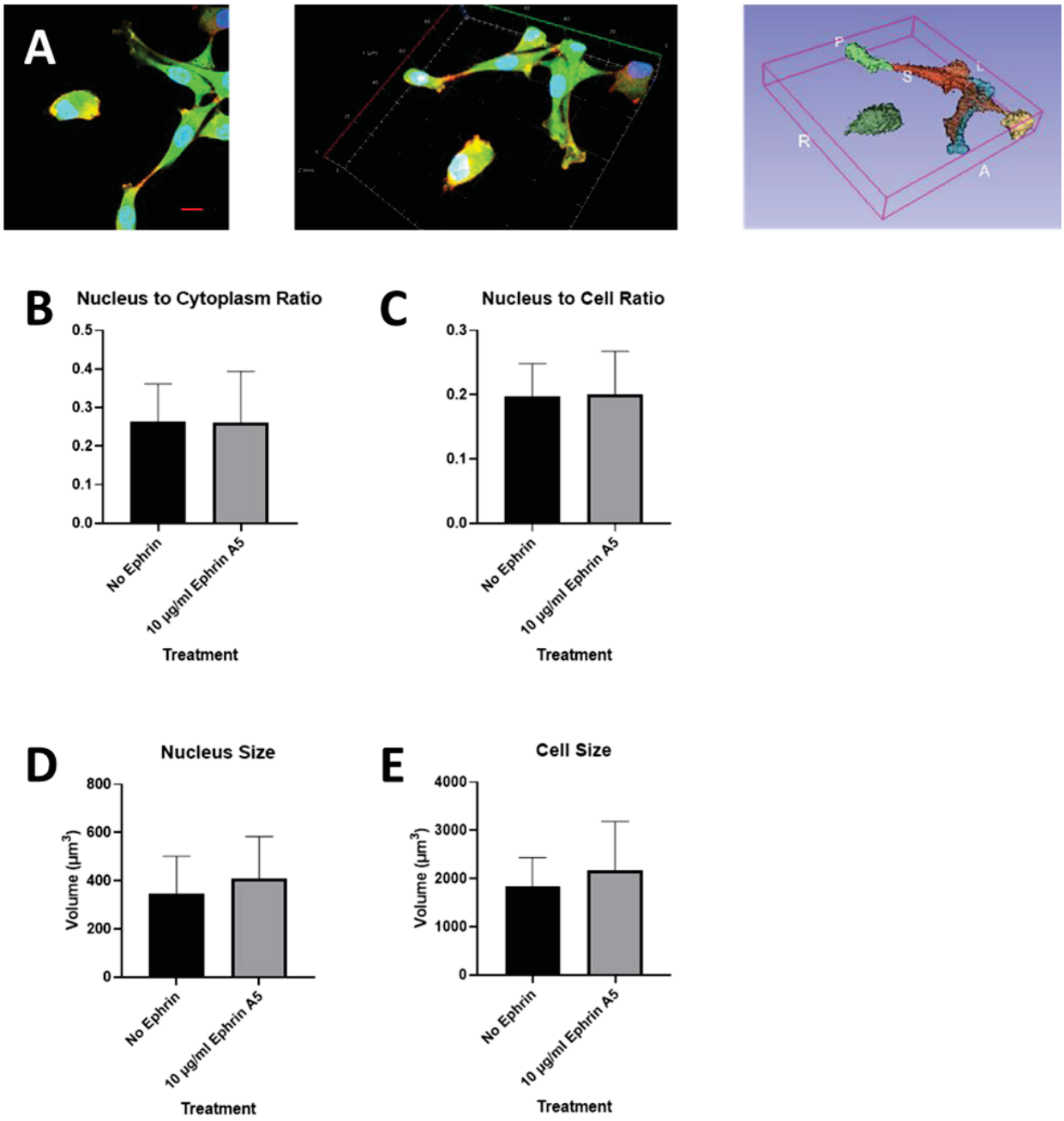

Figure 5.3. Cell compartment volume reconstructions from confocal microscopy. $F98_{BL}$ cells grown in two-dimensional culture were treated with 10 µg/ml ephrin A5 or ephrin-free growth medium. They were stained for actin (phalloidin-A555) and nuclei (DAPI), imaged, and reconstructed using Slicer software; scale bar denotes 100 µm (A). No significant differences were observed in nucleus-to-cytoplasm volumetric ratio (B), nucleus-to-cell volumetric ratio (C), nucleus size (D), or cell size (E).

healthy and malignant cells ($p < 0.05$). For a 2-5-2 burst scheme, the lethal EFT for $F98_{BL}$ cells ($n = 5$) was 1,249 ± 112 V/cm, which was not significantly different from the lethal EFT for DI TNC1 cells ($n = 5$), 1,436 ± 293 V/cm (Figure 5.1F). For a 5-1-5 burst scheme, the lethal EFT for $F98_{BL}$ cells ($n = 5$) was 941 ± 91 V/cm, while the lethal EFT for DI TNC1 cells ($n = 5$) was 1,164 ± 122 V/cm (Figure 5.1G). The lethal EFTs for the 5-1-5 pulse scheme were significantly different between healthy and malignant cells ($p < 0.05$). For a 5-2-5 burst scheme, the lethal EFT for $F98_{BL}$ cells ($n = 5$) was 949 ± 98 V/cm, while the lethal EFT for DI TNC1 cells ($n = 5$) was 1,087 ± 52 V/cm (Figure 5.1H). The lethal EFTs for the 5-2-5 pulse scheme were significantly different between healthy and malignant cells ($p < 0.05$). For a 5-5-5 burst scheme, the lethal EFT for $F98_{BL}$ cells ($n = 9$) was 992 ± 94 V/cm, which was not significantly different from the lethal EFT for DI TNC1 cells ($n = 5$), 1,075 ± 67 V/cm (Figure 5.1I). For a 10-1-10 burst scheme, the lethal EFT for $F98_{BL}$ cells ($n = 5$) was 772 ± 51 V/cm, which was not significantly different from the lethal EFT for DI TNC1 cells ($n = 5$), 873 ± 131 V/cm (Figure 5.1J).

H-FIRE Electric Field Thresholds in Response to Pre-Treatment with Ephrin

When $F98_{BL}$ and DI TNC1 cells were exposed to ephrin A1 or ephrin A5 for twelve hours prior to pulsing, the lethal EFTs were significantly lower for $F98_{BL}$ cells than DI TNC1 cells (Figure 5.2). In response to 1 μg/ml ephrin A1, $F98_{BL}$ cells ($n = 8$) were lethally ablated at 1139 ± 62 V/cm, while DI TNC1 cells ($n = 7$) were lethally ablated at 1288 ± 66 V/cm. For cells treated with 1 μg/ml ephrin A5, the lethal EFTs were 1172 ± 73 for $F98_{BL}$ cells ($n = 11$) and 1352 ± 46 V/cm for DI TNC1 cells ($n = 9$). A 2-way ANOVA detected a significant difference in both factors (no significant interaction detected; ephrin species factor difference detected, $p < 0.05$; cell type factor difference detected, $p < 0.0001$). Within cell types, no significant differences

were detected by post-hoc Sidak's test between ephrin species administered ($F98_{BL}$: $p = 0.46$; DI TNC1: $p = 0.10$). However, post-hoc tests detected significant differences between cell types within ephrin species: $F98_{BL}$ cells were lethally ablated at a significantly lower EFT following treatment with ephrin A1 ($p = 0.0001$) and following treatment with ephrin A5 ($p < 0.0001$).

Morphological Response to Ephrin

Three-dimensional morphology of $F98_{BL}$ cells was measured following 10 μg/ml ephrin A5 pre-treatment or exposure to vehicle control. Z-stacks were taken of cells in 2D culture and cellular and nuclear volumes were reconstructed and quantified in Slicer. The nucleus-to-cytoplasm ratio for $F98_{BL}$ cells treated with ephrin ($n = 30$) was 0.261 ± 0.133; for cells treated with control ($n = 30$), it was 0.263 ± 0.099 (Figure 5.3B). The nucleus-to-cell ratio, which did not subtract nuclear volume from cell volume, was 0.200 ± 0.167 for ephrin-treated cells ($n = 30$) and 0.197 ± 0.051 for cells without exogenous ephrin application ($n = 30$) (Figure 5.3C). Nuclear volumes were also compared: cells given the ephrin A5 treatment ($n = 35$) had nuclear volumes of 410 ± 173 μm^3, while control cells ($n = 34$) had nuclear volumes of 348 ± 154 μm^3 (Figure 5.3D). Finally, cell size was investigated; ephrin-treated cells ($n = 30$) were measured to be $2{,}165 \pm 1{,}021$ μm^3, while control cells ($n = 30$) were sized $1{,}830 \pm 610$ μm^3 (Figure 5.3E). No significant differences in nucleus-to-cytoplasm volume ratio were observed in the 3D reconstructions of the 2D-cultured $F98_{BL}$ cells treated with 10 μg/ml ephrin A5, as compared to cells fixed after being in ephrin-free medium. Neither was a significant difference seen in nucleus-to-cell volume ratio, nuclear volume, or cell volume.

Discussion

$F98_{BL}$ and DI TNC1 cells were treated with H-FIRE using 750 V pulse amplitude with 100 μs on-time per burst for 100, 1 Hz bursts. Under these conditions, the lethal EFT observed was lower for $F98_{BL}$ cells than DI TNC1 cells for every waveform tested. The $F98_{BL}$ EFT was statistically significantly lower for the 1-5-1, 2-2-2, 5-1-5, 5-2-5 ($p < 0.05$), and 2-1-2 ($p < 0.005$) pulse schemes, when compared to the corresponding DI TNC1 EFT. Selectivity for many pulse schemes was clear from visual analysis, as well, as many pulse schemes produced a DI TNC1 lesion that amounted to little more than the cylindrical holes in the gel where electrodes had been inserted with adjacent zones of dead cell staining that, if included in the area of the insertion track, would hardly have changed its diameter.

There is one slight issue with the lethal H-FIRE EFT data. It was conducted using two different generators, one of which, the H-FIRE 1.0, was observed to have some difficulty generating shorter (~1 μs) pulse widths. For short pulses, the step down from peak voltage is closer to an exponential decay function than the usual negative step function. This could cause a programmed 1-5-1 waveform to potentially be experienced as perhaps closer to a 1.5-4.5-1.5 waveform, though it should be noted that the leading edge that extends a fraction of a microsecond extends for the bulk of its time domain at an amplitude much closer to $0*V_{MAX}$ than to $1*V_{MAX}$, or a 2-2-2 programmed waveform as a 2.15-1.85-2.15 waveform. The EPULSUS-FBMI-5 has no such difficulties reliably generating shorter duration pulses. It is also important to note that almost every combination of pulse scheme and cell line contains data from both generators. Besides this inconsistency, all experimental conditions are identical. The overwhelmingly observed trend of lower lethal EFTs, which applies for schemes with 1 μs and 2 μs pulse widths, as well as others, supports that H-FIRE selectively targets $F98_{BL}$ cells given the above conditions.

As ephrin A1 exposure has previously been associated with larger lesions for malignant human cells but unchanged lesions in healthy human cells, we were interested in observing $F98_{BL}$ and DI TNC1 H-FIRE lesions following pre-treatment with both ephrin A1 and ephrin A5, as the latter is a component of QUAD. Following exposure to ephrin A1, $F98_{BL}$ cells had a significantly lower lethal H-FIRE EFT than DI TNC1 cells; the same was true for ephrin A5. As the ephrin-free data used 50 bursts and the post-ephrin H-FIRE treatment used 100 bursts, the data is not directly comparable. However, one would not expect the application of additional bursts to increase the lethal EFT. The EFT observed for $F98_{BL}$ cells is not increased, but the means measured are only marginally lower; all are between 1,100 and 1,200 V/cm. DI TNC1 cells' measured EFT decreases from over 1,600 V/cm to around 1,300 V/cm when ephrin pre-treatment is added and the burst number is increased. Future studies without confounding variables are needed to definitively state what, if any, effect ephrin A1 and ephrin A5 have on $F98_{BL}$ and healthy cell lethal H-FIRE EFTs. Nevertheless, it can be said that under the experimental treatments that we applied, H-FIRE selectivity is maintained in the presence of ephrin. The over 150 V/cm difference in lethal EFT would allow for versatility in treatment planning with the aim of imposing anti-GBM selectivity in *in vivo* applications.

It has been previously observed that an increase in nucleus-to-cytoplasm volume ratio for human GBM cells corresponded to a decrease in lethal EFT following ephrin treatment[29]. We therefore wished to investigate whether ephrin induced changes in nucleus-to-cytoplasm ratio in human cells. We cultured cells outside of a collagen matrix to allow unrestricted cell growth and standard cell adhesion, took z-stack confocal microscopy images of the nucleus and the actin cytoskeleton, which demarcates the cell boundaries, and reconstructed those images into quantifiable volumes. No significant differences were found in nucleus-to-cytoplasm ratio.

Neither was any significant difference detected for nucleus-to-cell volumetric ratio. It has been postulated that nuclear size, rather than nucleus-to-cytoplasm ratio, is what underlies the change in H-FIRE EFT observed in human GBM cells[27]. However, no differences were observed in nuclear volume either. Cellular volume was compared as well, and no differences were observed. The lack of observed morphological response to ephrin represents a divergence between ephrin A5-treated $F98_{BL}$ and ephrin A1-treated U251 and other human GBM model cell lines. It is unclear why no changes in morphology of cell compartment size were observed in response to high concentrations of ephrin A5. It is possible that only ephrin A1 has this effect; z-stack images were also collected of nuclear and cellular volumetric response to varying concentrations of ephrin A1, though the time-consuming process of reconstructing and quantifying cell compartment volumes has not yet been conducted. Another possible explanation is that the relatively high levels of ephrin A1 transcribed by $F98_{BL}$ cells automatically effects the morphological changes associated with ephrin A1 on GBM-like cells; this hypothesis is supported by the very high EPH A2 expression on the $F98_{BL}$ cell surface (see Chapter 3). It is also possible that other cell-line-specific peculiarities of the $F98_{BL}$ phenotype are the reason why no morphological differences are observed. If indeed ephrin does not enhance $F98_{BL}$ lesion areas in response to H-FIRE, which remains to be confirmed, then the fact that no morphological changes were observed may support a morphological mechanism underlying the ephrin-enhanced H-FIRE selectivity observed in human GBM cells. Conversely, if ephrin does indeed enhance $F98_{BL}$ lesion areas in response to H-FIRE, which also remains to be confirmed, then the lack of effect that ephrin A5 has on malignant cell morphology with respect to compartmental sizes may support a non-morphological mechanism of ephrin-enhanced H-FIRE selectivity in human GBM cells.

This is not the only divergence from what has been observed for human GBM cells. All lethal EFT data generated for this work, save those using a 10-1-10 waveform, has shown H-FIRE lethal EFTs greater than 900 V/cm, including in ephrin-treated gels, which is notable seeing as all work published by Ivey[29] shows thresholds lower than 750 V/cm for human GBM cells, with astrocyte lethal EFTs also lower, despite Ivey's use of a lower applied voltage and, in some cases, fewer bursts applied. This suggests that astrocyte-derived rat cells may have a generally higher resiliency to H-FIRE ablation than astrocyte-derived human cells. Nevertheless, the selectivity of H-FIRE that was observed to target human GBM cells likewise selectively targets $F98_{BL}$ cells.

Chapter 6: Discussion

Summary

Using multiple procedures to select for higher luciferase expression, I have established a bioluminescent F98 cell line that has a higher *in vitro* luminescent signal than any previously published. This confers additional benefits to the inherit invasiveness and low immunogenicity associated with F98 cells. Higher luminescent signal will increase the resolution of on-demand observation of tumor growth and improve subject quality of life.

While there was little difference in transcription of three of the targets of QUAD, EPH A3, EPH B2, and IL-13Rα2, between $F98_{BL}$ and DI TNC1 cells, EPH A2 transcription was higher in $F98_{BL}$ cells than DI TNC1 cells, as measured by PCR. Overexpression of EPH A2 alone is enough for QUAD targeting, due both to the design of QUAD as well as greater transcription of all of the receptors of ephrin A5. Furthermore, EPH A2 was present more ubiquitously and more densely on the surface of $F98_{BL}$ cells than DI TNC1 cells, as observed by immunocytochemical staining. Given the high prevalence of EPH A2 on $F98_{BL}$, QUAD-CTX binding is a likely outcome of contact between the ephrin A5 component of QUAD and the $F98_{BL}$ cell surface. The viability of $F98_{BL}$ cells decreased with increasing doses of QUAD-WP396 administered; this could not be said for DI TNC1 cells. The IC_{50} dose of QUAD-WP396 for limiting $F98_{BL}$ viability was 2.348 nM, placing it within the range observed for human GBM cells[40]. The viability curves for $F98_{BL}$ and DI TNC1 cells indicate that a treatment between 10 nM and 100 nM will kill nearly all $F98_{BL}$ cells while preserving bulk astrocytic tissue.

Blood-brain barrier disruption volume decreased exponentially with time, with complete recovery occurring by 96 hours. The first areas to regain BBB integrity are the most distal from treatment, with the area surrounding the electrodes experiencing the longest BBBD. This feature may be useful when designing patient-specific treatments. The molecular sizes of our BBB-impenetrable markers used to quantify BBBDV were of comparable size to doxorubicin and to QUAD-CTX; no difference in BBBDV at a given timepoint was observed between marker sizes. EFT required for local BBBD increased with respect to BBBD duration following a sigmoidal curve. This observation is useful for treatment planning as well.

$F98_{BL}$ cells were lethally ablated at lower EFTs than rat phenotype 1 astrocytes under the H-FIRE pulse parameters applied. $F98_{BL}$ cells also were ablated at significantly lower lethal EFTs by H-FIRE than DI TNC1 cells following pre-treatment with ephrin. H-FIRE can selectively target $F98_{BL}$ cells in the presence or the absence of ephrin. However, ephrin A5 was not found to induce any morphological changes in $F98_{BL}$ cells, whether in nuclear volume or nucleus-to-cytoplasm volumetric ratio.

Future Work

Additional future *in vitro* work should include analysis of protein-level translation of QUAD targets and of pathway-related proteins. Gene expression in 3D culture is also another avenue for potential investigation that would more closely mimic the microenvironment relevant to the *in vivo* experiments. More work will also be needed to investigate the toxicity of QUAD-WP396 doses between 10 nM and 100 nM, as well as to determine what concentration of injection will result in the appropriate dose being present in the brain parenchyma. The ability to directly compare lethal H-FIRE EFTs with and without ephrin pre-treatment will be gained by

conducting the following experiment. $F98_{BL}$ and DI TNC1 cells cultured separately in hydrogels will receive H-FIRE treatment with pulse parameters set to include both 50 and 100 bursts of a 750 V, 1 Hz, 100 μs on-time bursts, delivered in a 1-5-1 pulse scheme by the EPULSUS-FBMI-5[53] generator. The lesion sizes will be quantified and, from these, lethal EFTs will be calculated. Additional hydrogel treatments will seed $F98_{BL}$ and DI TNC1 cells in a co-culture; this will enable the study of the effects of their differing endogenous ephrin expression on each other's lethal EFTs and morphology.

Some future work is best conducted without using 3D tissue hydrogel models. In one experiment I attempted, I pre-treated $F98_{BL}$ cells and DI TNC1 cells with QUAD-WP396 prior to the application of H-FIRE in hydrogels. It was not very successful, and it proved the impracticality of applying QUAD-CTX to cells grown in the hydrogel construction conventionally employed by our research group. QUAD-WP396 is not readily available in large quantities, of the sort required to cover tens of hydrogels with 500 μl of 1 - 100 nM QUAD-WP396. Nevertheless, we will study a combinatorial therapy *in vitro* before we study it *in vivo*. Another experimental platform will be used, whether it take the form of smaller hydrogels, cells suspended in cuvettes, or another innovative experimental design.

The most obvious future work will be to implant these $F98_{BL}$ cells orthotopically into Fischer rats and characterize their growth dynamics. Indeed, that work will take place nearly concurrently with the final submission deadline of this thesis. Pending that characterization, testing will proceed to study strongly ablative H-FIRE, minimally ablative H-FIRE, liposomal doxorubicin, and QUAD-Dox, as well as combinatorial therapies building on those fundamental therapies in pre-clinical trials.

Importance

The two constituent therapies of our proposed combinatorial therapy, H-FIRE and QUAD-CTX, support each other and target GBM in multiple ways. HFE disrupts the BBB, which should enable QUAD-CTX, as well as unconjugated chemotherapeutic agents, to permeate the brain parenchyma surrounding the tumor. The BBBD temporal window lasts for days, which enables repeated administration of targeting agents. There is also the targeting by H-FIRE itself, which has been proven capable of selectively targeting GBM and GBM-like cells. The immune response mediated by H-FIRE may also provide selective targeting by the host's own immune system. These two treatments may also be used in combination with surgical resection, traditional chemotherapy, and radiotherapy.

Many cancer therapies generally and GBM therapies specifically have shown promise in early testing but have failed in clinical trials. This highlights the importance of tailoring pre-clinical conditions as closely as possible to the intended endpoint patient who may stand to benefit from a treatment. The model I have developed is the product of great effort to make it as directly translatable to clinical trials as possible. With this effort invested and the model proven apt, it may become another pillar to support the success that our promising combinatorial therapeutic approach may have in thoroughly and selectively ablating glioblastoma tumors. The manifold modalities available for treating GBM patients, when tested within appropriate, translatable models, have the potential to improve GBM prognosis more dramatically than the advances of decades of work.

Chapter 7: Conclusion

Bioluminescent F98 cells were selectively targeted by both H-FIRE and QUAD-WP396, which HFE enables to permeate the blood-brain barrier. In showing this, I have established a versatile and accurate *in vivo* model that will allow us to test the efficacy of a selective combinatorial treatment against human glioblastoma multiforme. If a novel treatment is to ever break through and meaningfully improve GBM prognoses, it is crucial that its pre-clinical trials be conducted in a way that is truly predictive of the response by real, suffering patients. For this promising therapeutic strategy, my model is the way.

Reference List

1. Ostrom QT, Cioffi G, Gittleman H, et al. CBTRUS Statistical Report: Primary Brain and Other Central Nervous System Tumors Diagnosed in the United States in 2012-2016. *Neuro Oncol*. 2019;21(Suppl 5):v1-v100. doi:10.1093/neuonc/noz150

2. Inda MM, Bonavia R, Seoane J. Glioblastoma multiforme: a look inside its heterogeneous nature. *Cancers (Basel)*. 2014;6(1):226-239. Published 2014 Jan 27. doi:10.3390/cancers6010226

3. Scherer HJ. Structural Development in Gliomas. *Cancer Res.* 1938;34(3):333-351. Published 1938 Nov 1. doi:10.1158/ajc.1938.333

4. Rezaei V, Rabiee A, Khademi F. Glioblastoma multiforme: a glance at advanced therapies based on nanotechnology. *J Chemother*. 2020;32(3):107-117. doi:10.1080/1120009X.2020.1713508

5. Kanu OO, Mehta A, Di C, et al. Glioblastoma multiforme: a review of therapeutic targets. *Expert Opin Ther Targets*. 2009;13(6):701-718. doi:10.1517/14728220902942348

6. Gilbert MR, Dignam JJ, Armstrong TS, et al. A randomized trial of bevacizumab for newly diagnosed glioblastoma. *N Engl J Med*. 2014;370(8):699-708. doi:10.1056/NEJMoa1308573

7. Debinski W, Priebe W, Tatter SB. Maximizing Local Access to Therapeutic Deliveries in Glioblastoma. Part I: Targeted Cytotoxic Therapy. In: De Vleeschouwer S, ed. *Glioblastoma*. Brisbane (AU): Codon Publications; September 27, 2017.

8. Edd JF, Horowitz L, Davalos RV, Mir LM, Rubinsky B. In vivo results of a new focal tissue ablation technique: irreversible electroporation. *IEEE Trans Biomed Eng*. 2006;53(7):1409-1415. doi:10.1109/TBME.2006.873745

9. Rubinsky B, Onik G, Mikus P. Irreversible electroporation: a new ablation modality--clinical implications. *Technol Cancer Res Treat*. 2007;6(1):37-48. doi:10.1177/153303460700600106

10. Guenther E, Klein N, Zapf S, et al. Prostate cancer treatment with Irreversible Electroporation (IRE): Safety, efficacy and clinical experience in 471 treatments. *PLoS One*. 2019;14(4):e0215093. Published 2019 Apr 15. doi:10.1371/journal.pone.0215093

11. Martin RC 2nd, Kwon D, Chalikonda S, et al. Treatment of 200 locally advanced (stage III) pancreatic adenocarcinoma patients with irreversible electroporation: safety and efficacy. *Ann Surg*. 2015;262(3):486-494. doi:10.1097/SLA.0000000000001441

12. Bhutiani N, Philips P, Scoggins CR, McMasters KM, Potts MH, Martin RC. Evaluation of tolerability and efficacy of irreversible electroporation (IRE) in treatment of Child-Pugh B (7/8) hepatocellular carcinoma (HCC). *HPB (Oxford)*. 2016;18(7):593-599. doi:10.1016/j.hpb.2016.03.609

13. Aycock KN, Davalos RV. Irreversible Electroporation: Background, Theory, and Review of Recent Developments in Clinical Oncology. *Bioelectricity*. 2019;1(4):214-234. doi:10.1089/bioe.2019.0029

14. Böckmann RA, de Groot BL, Kakorin S, Neumann E, Grubmüller H. Kinetics, statistics, and energetics of lipid membrane electroporation studied by molecular dynamics simulations. *Biophys J*. 2008;95(4):1837-1850. doi:10.1529/biophysj.108.129437

15. Okino M, Mohri H. Effects of a high-voltage electrical impulse and an anticancer drug on in vivo growing tumors. *Jpn J Cancer Res*. 1987;78(12):1319-1321.

16. Mir LM, Orlowski S, Belehradek J Jr, Paoletti C. Electrochemotherapy potentiation of antitumour effect of bleomycin by local electric pulses. *Eur J Cancer*. 1991;27(1):68-72. doi:10.1016/0277-5379(91)90064-k

17. Prausnitz MR, Bose VG, Langer R, Weaver JC. Electroporation of mammalian skin: a mechanism to enhance transdermal drug delivery. *Proc Natl Acad Sci U S A*. 1993;90(22):10504-10508. doi:10.1073/pnas.90.22.10504

18. Lohr F, Lo DY, Zaharoff DA, et al. Effective tumor therapy with plasmid-encoded cytokines combined with in vivo electroporation. *Cancer Res*. 2001;61(8):3281-3284.

19. Titomirov AV, Sukharev S, Kistanova E. In vivo electroporation and stable transformation of skin cells of newborn mice by plasmid DNA. *Biochim Biophys Acta*. 1991;1088(1):131-134. doi:10.1016/0167-4781(91)90162-f

20. Garcia PA, Rossmeisl JH Jr, Neal RE 2nd, et al. Intracranial nonthermal irreversible electroporation: in vivo analysis. *J Membr Biol*. 2010;236(1):127-136. doi:10.1007/s00232-010-9284-z

21. Bonakdar M, Graybill PM, Davalos RV. A microfluidic model of the blood-brain barrier to study permeabilization by pulsed electric fields. *RSC Adv*. 2017;7(68):42811-42818. doi:10.1039/C7RA07603G

22. Sharabi S, Bresler Y, Ravid O, et al. Transient blood-brain barrier disruption is induced by low pulsed electrical fields in vitro: an analysis of permeability and trans-endothelial

electric resistivity. *Drug Deliv*. 2019;26(1):459-469. doi:10.1080/10717544.2019.1571123

23. Ball C, Thomson KR, Kavnoudias H. Irreversible electroporation: a new challenge in "out of operating theater" anesthesia. *Anesth Analg*. 2010;110(5):1305-1309. doi:10.1213/ANE.0b013e3181d27b30

24. Arena CB, Sano MB, Rossmeisl JH Jr, et al. High-frequency irreversible electroporation (H-FIRE) for non-thermal ablation without muscle contraction. *Biomed Eng Online*. 2011;10:102. Published 2011 Nov 21. doi:10.1186/1475-925X-10-102

25. Ringel-Scaia VM, Beitel-White N, Lorenzo MF, et al. High-frequency irreversible electroporation is an effective tumor ablation strategy that induces immunologic cell death and promotes systemic anti-tumor immunity. *EBioMedicine*. 2019;44:112-125. doi:10.1016/j.ebiom.2019.05.036

26. Latouche EL, Arena CB, Ivey JW, et al. High-Frequency Irreversible Electroporation for Intracranial Meningioma: A Feasibility Study in a Spontaneous Canine Tumor Model. *Technol Cancer Res Treat*. 2018;17:1533033818785285. doi:10.1177/1533033818785285

27. Ivey JW, Wasson EM, Alinezhadbalalami N, Kanitkar A, Debinski W, Sheng Z, Davalos RV, Verbridge SS. Characterization of Ablation Thresholds for 3D-Cultured Patient-Derived Glioma Stem Cells in Response to High-Frequency Irreversible Electroporation. *Research (Wash D.C.)*. 2019 Apr 4;2019:8081315. doi:10.34133/2019/8081315

28. Ivey JW, Latouche EL, Sano MB, Rossmeisl JH, Davalos RV, Verbridge SS. Targeted cellular ablation based on the morphology of malignant cells. *Sci Rep*. 2015;5:17157. Published 2015 Nov 24. doi:10.1038/srep17157

29. Ivey JW, Latouche EL, Richards ML, et al. Enhancing Irreversible Electroporation by Manipulating Cellular Biophysics with a Molecular Adjuvant. *Biophys J*. 2017;113(2):472-480. doi:10.1016/j.bpj.2017.06.014

30. Wykosky J, Gibo DM, Stanton C, Debinski W. Interleukin-13 receptor alpha 2, EphA2, and Fos-related antigen 1 as molecular denominators of high-grade astrocytomas and specific targets for combinatorial therapy. *Clin Cancer Res*. 2008;14(1):199-208. doi:10.1158/1078-0432.CCR-07-1990

31. Boyd AW, Bartlett PF, Lackmann M. Therapeutic targeting of EPH receptors and their ligands. *Nat Rev Drug Discov*. 2014;13(1):39-62. doi:10.1038/nrd4175

32. Ferluga S, Tomé CM, Herpai DM, D'Agostino R, Debinski W. Simultaneous targeting of Eph receptors in glioblastoma. *Oncotarget*. 2016;7(37):59860-59876. doi:10.18632/oncotarget.10978

33. Nakada M, Niska JA, Miyamori H, et al. The phosphorylation of EphB2 receptor regulates migration and invasion of human glioma cells. *Cancer Res*. 2004;64(9):3179-3185. doi:10.1158/0008-5472.can-03-3667

34. Wykosky J, Gibo DM, Debinski W. A novel, potent, and specific ephrinA1-based cytotoxin against EphA2 receptor expressing tumor cells. *Mol Cancer Ther*. 2007;6(12 Pt 1):3208-3218. doi:10.1158/1535-7163.MCT-07-0200

35. Wynn TA. IL-13 effector functions. *Annu Rev Immunol*. 2003;21:425-456. doi:10.1146/annurev.immunol.21.120601.141142

36. Wills-Karp M, Finkelman FD. Untangling the complex web of IL-4- and IL-13-mediated signaling pathways. *Sci Signal*. 2008;1(51):pe55. Published 2008 Dec 23. doi:10.1126/scisignal.1.51.pe55

37. Suzuki A, Leland P, Joshi BH, Puri RK. Targeting of IL-4 and IL-13 receptors for cancer therapy. *Cytokine*. 2015;75(1):79-88. doi:10.1016/j.cyto.2015.05.026

38. Debinski W, Gibo DM, Obiri NI, Kealiher A, Puri RK. Novel anti-brain tumor cytotoxins specific for cancer cells. *Nat Biotechnol*. 1998;16(5):449-453. doi:10.1038/nbt0598-449

39. Mintz A, Gibo DM, Slagle-Webb B, Christensen ND, Debinski W. IL-13Ralpha2 is a glioma-restricted receptor for interleukin-13. *Neoplasia*. 2002;4(5):388-399. doi:10.1038/sj.neo.7900234

40. Sharma P, Sonawane P, Herpai D, D'Agostimo R, Rossmeisl J, Tatter S, Debinski W. Multi-receptor targeting of glioblastoma. *Neuro-oncol adv*. 2020;Accepted Manuscript. Published 2020 Aug 26. doi:10.1093/noajnl/vdaa107

41. Hjouj M, Last D, Guez D, et al. MRI study on reversible and irreversible electroporation induced blood brain barrier disruption. *PLoS One*. 2012;7(8):e42817. doi:10.1371/journal.pone.0042817

42. Sharabi S, Last D, Guez D, et al. Dynamic effects of point source electroporation on the rat brain tissue. *Bioelectrochemistry*. 2014;99:30-39. doi:10.1016/j.bioelechem.2014.06.001

43. Darling TK, Lamb TJ. Emerging Roles for Eph Receptors and Ephrin Ligands in Immunity. *Front Immunol.* 2019 Jul 4;10:1473. doi: 10.3389/fimmu.2019.01473.

44. Tzeng JJ, Barth RF, Orosz CG, James SM. Phenotype and functional activity of tumor-infiltrating lymphocytes isolated from immunogenic and nonimmunogenic rat brain tumors. *Cancer Res*. 1991;51(9):2373-2378.

45. Barth RF, Kaur B. Rat brain tumor models in experimental neuro-oncology: the C6, 9L, T9, RG2, F98, BT4C, RT-2 and CNS-1 gliomas. *J Neurooncol*. 2009;94(3):299-312. doi:10.1007/s11060-009-9875-7

46. Bryant MJ, Chuah TL, Luff J, Lavin MF, Walker DG. A novel rat model for glioblastoma multiforme using a bioluminescent F98 cell line. *J Clin Neurosci*. 2008;15(5):545-551. doi:10.1016/j.jocn.2007.04.022

47. Huang FY, Lee TW, Chang CH, et al. Evaluation of 188Re-labeled PEGylated nanoliposome as a radionuclide therapeutic agent in an orthotopic glioma-bearing rat model. *Int J Nanomedicine*. 2015;10:463-473. Published 2015 Jan 9. doi:10.2147/IJN.S75955

48. Mowday AM, Lieuwes NG, Biemans R, et al. Use of a Luciferase-Expressing Orthotopic Rat Brain Tumor Model to Optimize a Targeted Irradiation Strategy for Efficacy Testing with Temozolomide. *Cancers (Basel)*. 2020;12(6):1585. Published 2020 Jun 15. doi:10.3390/cancers12061585

49. Mathieu D, Lecomte R, Tsanaclis AM, Larouche A, Fortin D. Standardization and detailed characterization of the syngeneic Fischer/F98 glioma model. *Can J Neurol Sci*. 2007;34(3):296-306. doi:10.1017/s0317167100006715

50. Ben-David U, Siranosian B, Ha G, et al. Genetic and transcriptional evolution alters cancer cell line drug response. *Nature*. 2018;560(7718):325-330. doi:10.1038/s41586-018-0409-3

51. Wykosky J, Gibo DM, Stanton C, Debinski W. EphA2 as a novel molecular marker and target in glioblastoma multiforme. *Mol Cancer Res*. 2005;3(10):541-551. doi:10.1158/1541-7786.MCR-05-0056

52. Lorenzo MF, Thomas SC, Kani Y, et al. Temporal Characterization of Blood-Brain Barrier Disruption with High-Frequency Electroporation. *Cancers (Basel)*. 2019;11(12):1850. Published 2019 Nov 23. doi:10.3390/cancers11121850

53. Redondo LM, Zahyka M, Kandratsyeu A. Solid-State Generation of High-Frequency Burst of Bipolar Pulses for Medical Applications. *IEEE Trans Plasma Sci IEEE Nucl Plasma Sci Soc*. 2019;47(8):4091-4095. Doi:10.1109/TPS.2019.2923570.

54. Arena CB, Szot CS, Garcia PA, Rylander MN, Davalos RV. A three-dimensional in vitro tumor platform for modeling therapeutic irreversible electroporation. *Biophys J.* 2012;103(9):2033-2042. doi:10.1016/j.bpj.2012.09.017

Appendix A

Matlab Code Referenced in Chapter 4

```
close all

clear all

clc



% Define EFs

EF = (1:1:2000);

% Load Area vs. EFT COMSOL

load('vthreshes.mat');

% Load my experimental data, should be 104 points. This is a CSV in

% column form.

PutTheAreaValueHere = csvread('Ablationareas.csv');

% Conver to an arry

areas = table2array(vthreshes(:,2))';

% Take x and y data and fit an nth order polynomial

x  = areas;

y = EF;
```

```
n = 5;

p = polyfit(x,y,n);

% Define the fitted function, with x as the experimental ablation area

field = @(inputarea)
p(1)*inputarea^(5)+p(2)*inputarea^(4)+p(3)*inputarea^(3)+p(4)*inputarea^(2)+p(5)*inp
utarea+p(6);

% Evaluate the fit with the experimental data

for i = 1 : length(PutTheAreaValueHere)

    EFTall(i) = field(PutTheAreaValueHere(i));

    fprintf('The EF threshold is %.2f V/cm \n', EFTall(i))

end



csvwrite('AblationEFTs.csv',EFTall')
```